JAERI-M
92-022

PROGRESS REPORT ON SAFETY RESEARCH ON HIGH-LEVEL WASTE MANAGEMENT FOR THE PERIOD APRIL 1990 TO MARCH 1991

March 1992

(Eds.) Susumu MURAOKA, Muneaki SENOO and Yoshii KOBAYASHI

日本原子力研究所
Japan Atomic Energy Research Institute

JAERI-Mレポートは，日本原子力研究所が不定期に公刊している研究報告書です。
入手の問合わせは，日本原子力研究所技術情報部情報資料課（〒319-11茨城県那珂郡東海村）あて，お申しこしください。なお，このほかに財団法人原子力弘済会資料センター（〒319-11茨城県那珂郡東海村日本原子力研究所内）で複写による実費頒布をおこなっております。

JAERI-M reports are issued irregularly.
Inquiries about availability of the reports should be addressed to Information Division Department of Technical Information, Japan Atomic Energy Research Institute, Tokai-mura, Naka-gun, Ibaraki-ken 319-11, Japan.

編集兼発行　日本原子力研究所
印　　刷　いばらき印刷㈱

JAERI-M 92-022

Progress Report on Safety Research on High-level Waste Management for the Period April 1990 to March 1991

(Eds.) Susumu MURAOKA, Muneaki SENOO and Yoshii KOBAYASHI

Department of Environmental Safety Research
Tokai Research Establishment
Japan Atomic Energy Research Institute
Tokai-mura, Naka-gun, Ibaraki-ken

(Received January 30, 1992)

Research on high-level waste management at the Engineered Barrier Materials Laboratory, Environmental Geochemistry Laboratory and Environmental Radiochemistry Laboratory of the Department of Environmental Safety Research, JAERI in the fiscal year of 1990 are described.

The topics are as follows:

1) As for waste forms and engineered barrier material, performance assessment studies on glass, ceramic and buffer materials, and corrosion test of stainless steel were carried out.
2) In the safety evaluation study for geological disposal, chemical behavior of nuclide in water, nuclide migration and fixation in geosphere were studied.
3) Distribution of uranium and migration of uranium series nuclide in uranium ore were examined as a natural analogue study.

Keywords: High-level Waste, Waste Forms, Engineered Barrier Material, Glass, Ceramic, Migration, Retardation, Geosphere, Uranium, Natural Analogue, Progress Report

JAERI－M 92－022

高レベル廃棄物処理処分の安全性に関する平成２年度報告書

日本原子力研究所東海研究所環境安全研究部
（編）村岡　　進・妹尾　宗明・小林　義威

（1992年１月30日受理）

人工バリア研究室，深地処分研究室及び環境放射化学研究室において，平成２年度に実施した高レベル廃棄物処理処分の安全性に関する研究成果をまとめた。

その内容は次の通りである。

1）廃棄物固化体及び人工バリア材の研究開発では，ガラス固化体，セラミック固化体及び緩衝材の性能評価試験並びに容器材料の耐食性試験を継続した。

2）地層処分の安全評価試験では，核種の水中での化学的挙動，地層中での核種の移行・固定機構の研究を実施した。また，岩石中の元素の化学形分析法の開発を進めた。

3）ナチュラルアナログ研究として，ウラン鉱床中のウラン系列核種の移行及び分布に関する研究を実施した。

＊東海研究所：〒319-11　茨城県那珂郡東海村白方字白根2-4

Contents

目　　次

Introduction

In order to achieve the safe disposal of high-level radioactive waste, it is necessary to promote the development of waste management and safety assessment methodology.

The Japan Atomic Energy Research Institute (JAERI) has conducted safety assessment study and development of new technology to contribute the establishment of national system for the high-level radioactive waste management in Japan.

This report summarizes the status and results of studies performed in the fiscal year 1990 at the Engineered Barrier Materials Laboratory, Environmental Geochemistry Laboratory and Environmental Radiochemistry Laboratory of the Department of Environmental Safety Research, JAERI.

The progress report series have been issued in the following numbers; JAERI-M 82-145, 83-076, 84-133, 85-090, 86-131, 87-131, 88-201, 89-192 and 91-019.

1. Research and Development of Waste Forms and Engineered Barrier Materials

1.1 Performance of Glass Waste Forms

1.1.1 Effects of Some Glass Additives on Nuclear Waste Glass Durability in Water

H. Kamizono

In this study[1], we try to improve the durability of the HLW glass as much as possible. For this purpose, the effects of some glass additives on nuclear waste glass durability in water are examined. For example, Fe_2O_3 is used as a glass additive, since it has been found that Fe tends to concentrate on the glass surface during leaching and may act as a protective barrier against leaching. The addition of PbO is also examined, since leach rates of HLW glass have been reported to be low in Pb containers. The effects of GeO_2 are also observed since Ge is a network former and Ge-O-Ge polyhedra substitute part of the Si-O-Si network structure. Each of the above three oxides is added to HLW glass up to 20 wt%, and results of MCC-1 static leach experiments are discussed.

The simulated HLW glass which is borosilicate glass containing non-radioactive waste elements was used for this study as a standard glass. The reagents for base glass and waste elements were mixed simultaneously with up to 20 wt% of Fe_2O_3, PbO or GeO_2. Each mixture was melted at 1150°C for 2 hours, poured into a graphite mold, annealed at 550 to 660°C for 1 hour and then cooled to room temperature at a cooling rate of less than 1°C/min. The resultant glass blocks were cut, and polished slightly into cubic specimens of 8 × 8 × 8 mm in size. Nine kinds of glass were prepared for this study, which were identified as STD (standard), Fe-10 (7 wt% of Fe_2O_3 were added), Fe-20, Pb-5 (5 wt% of PbO were added), Pb-10, Pb-20, Ge-5 (5 wt% of GeO_2 were added), Ge-10 and Ge-20 (Table 1). It should be noted that about 3 wt% of Fe_2O_3 were originally contained in the STD glass and therefore 7 wt% of Fe_2O_3 were added to make the Fe-10 glass. Nine kinds of glass were characterized as amorphous by X-ray diffractometry.

The MCC-1 static leach tests on each glass were carried out at 70 ± 1°C for 14 and 28 days. Deionized water with a pH value of 5.6, an Eh value of +0.4 V and a specific resistance of more than 10^6 ohm·cm was

used as leachant. The pH of the leachates was measured with a pH electrode immediately upon cooling to room temperature. About 1 wt% of HNO_3 (13.4 M) was added to the part of the leachate. Concentrations of elements in the acidified leachates were analyzed by inductively-coupled plasma atomic emission spectroscopy or atomic adsorption spectroscopy. The surface of the specimens before and after the leach tests was observed with a scanning electron microscope (SEM) with energy dispersive X-ray analyses (EDX).

The results in Fig. 1 shows that the addition of Fe_2O_3 into the glass decreases normalized elemental mass losses (NL-values) for six elements studied. The addition of PbO into the glass decreases NL-values for B, Na and Si, on the other hand it increases NL-values for Ca, Ba, Fe and Pb. The addition of GeO_2 increases NL-values for seven elements studied. It was found by the SEM-EDX observation that Fe and Pb tended to enrich on the glass surface during leaching but Ge did not.

It is thought that the addition of Fe_2O_3 improves the glass durability. Hydroxides of Fe have low solubilities, resulting in the formation of a Fe rich surface layer on the glass. The Fe rich surface layer tends to serve as a protective barrier against leaching of other elements from the bulk to the outside solution. This tendency is clearly observed under the present experimental conditions, since Fe hydroxides are stable in alkaline and oxidized solutions.

PbO also tends to concentrate on the surface of the glass during leaching. It forms a protective surface layer, resulting in lower leach rates for B, Na and Si. However, Pb is stable as Pb carbonate ($PbCO_3$) or Pb hydroxyl carbonate ($2PbCO_3Pb(OH)_2$) in an alkaline solution. This prevents Ca and Ba from precipitating as carbonates and plays a role in increasing Ca and Ba concentrations in the leachates. It is also found that Fe in the leachates tends to increase as Pb in the glass increases, however this is not clearly explained at present.

The addition of GeO_2 makes the Si-O-Si network structure weaker under alkaline conditions, because GeO_2 dissolves in the form of $HGeO_3^-$ or GeO_3^{2-}. There are two polymorphs of GeO_2: One is stable at temperatures of more than 1033°C, and the other is stable at less than 1033°C. The former is insoluble and the latter is soluble in water. It is thought that during the vitrification process, the structure of GeO_2 stable at a lower temperature may be introduced and GeO_2 make the glass more soluble in water.

In conclusion, the leach rate of the STD glass used in this study is not so low as that of commercial HLW glass, however mechanisms involved are clear in that solubilities of Fe or Ge hydroxides into leachates influence the overall leaching behavior of HLW glass. Although effects of the PbO addition is not clearly understood at present, the formation of Pb carbonates in the leachates may effect in increase of the Ca and Ba concentrations in the leachates.

REFERENCE

(1) H. Kamizono et al., J. Mater. Sci. Lett., 10, 423-425 (1991).

Table 1 Composition of nine kinds of glass in wt%

Component	STD	Fe-10	Fe-20	Pb-5 Ge-5	Pb-10 Ge-10	Pb-20 Ge-20
Additives						
SiO_2	52.08	48.30	42.93	49.48	46.87	41.66
B_2O_3	22.70	21.05	18.71	21.57	20.43	18.16
Na_2O	11.22	10.41	9.25	10.66	10.10	8.98
Simulated high-level waste*						
K_2O	0.06	0.06	0.05	0.06	0.05	0.05
SrO	0.31	0.29	0.26	0.29	0.28	0.25
CaO**	1.43	1.33	1.18	1.36	1.29	1.14
ZrO_2	1.50	1.39	1.24	1.43	1.35	1.20
MoO_3	1.58	1.47	1.30	1.50	1.42	1.26
MnO_2	0.24	0.22	0.20	0.23	0.22	0.19
Fe_2O_3	2.96	10.00	20.00	2.81	2.66	2.37
CoO	0.11	0.10	0.09	0.10	0.10	0.09
NiO	0.60	0.56	0.49	0.57	0.54	0.48
TeO_2	0.21	0.19	0.17	0.20	0.19	0.17
Cs_2O	0.89	0.83	0.73	0.85	0.80	0.71
BaO	0.57	0.53	0.47	0.54	0.51	0.46
Na_2O	2.90	2.69	2.39	2.76	2.61	2.32
P_2O_5	0.29	0.27	0.24	0.28	0.26	0.23
Cr_2O_3	0.35	0.32	0.29	0.33	0.32	0.28
PbO or GeO_2	-	-	-	5.00	10.00	20.00

* This waste is called JW-C in our notation.

** Calcium simulates the actinides and the rate-earths in HLW.

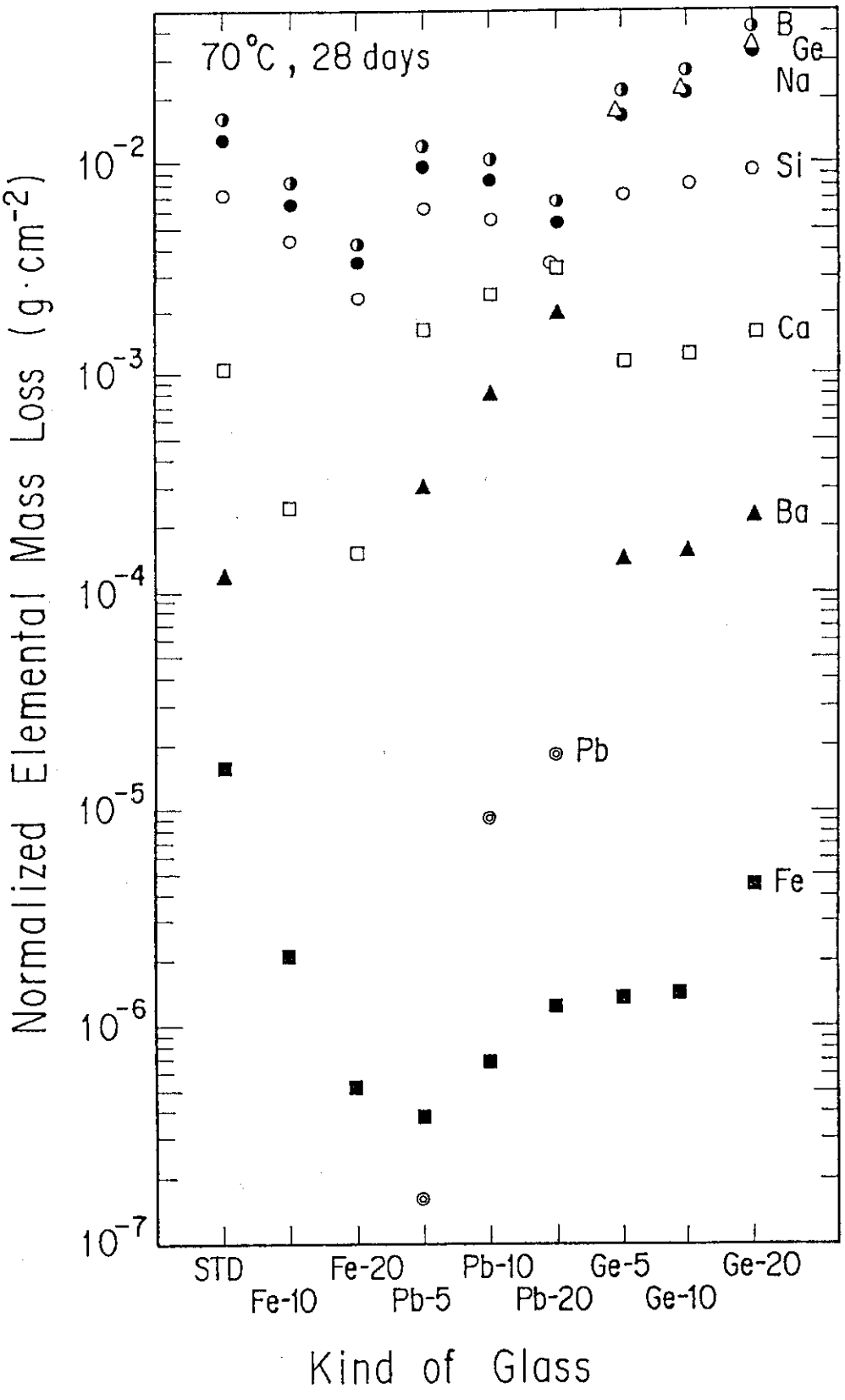

Fig. 1 Normalized elemental mass loss vs. kind of glass

1.2 Performance of Ceramic Waste Forms

1.2.1 Change in Density of Curium-doped Titanate Ceramic Containing Sodium-free High-level Nuclear Waste

H. Mitamura, S. Matsumoto and T. Tsuboi

INTRODUCTION

When volume swelling due to accumulation of alpha decays causes crack propagation in a polyphase titanate ceramic containing high-level nuclear waste[1], it leads to an increase in the effective surface area exposed to ground water. In addition, actinide-host phases have possibility to deteriorate their chemical durability due to the alpha-decay damage[2]. This means that the microencapsulation effect may be no longer effective once accumulation of alpha decays will cause crack propagation. In the previous study[2], the curium-doped sodium-bearing titanate ceramic showed a significant increase in the leach rates of soluble indicator elements after a dose of 9×10^{17} alpha decays$\cdot g^{-1}$ (equivalent age, ~10000 yr). Since a large amount of actinide nuclides will be still alive at this time, it is desirable that crack propagation will be suppressed as much as possible, to maintain the microencapsulation effect. The sodium content could be reduced with a minor change in the waste stream in a reprocessing plant. In the present study, we use typical sodium-free HLW so-called "PW-4b" waste to clarify effects of processing contaminants. The sodium-free titanate ceramic was doped with a short-lived actinide nuclide, ^{244}Cm ($T_{1/2}$=18.1 yr), to accelerate long-term self-irradiation due to alpha decays, and its density was measured.

EXPERIMENTAL METHODS

Sample Preparation

The nominal composition of the curium-doped PW-4b titanate ceramic is shown in Table 1. This waste contains less amount of inerts than the sodium-bearing waste designated "JW-A" waste. The curium-doped samples containing PW-4b waste was prepared as in the previous study[3].

Two batches of the slurry mixture of the precursor and simulated PW-4b waste were calcined at 750°C for 2 h under a stream of Ar+4%H_2 gas

using a hot-cell apparatus. The mixture of the calcined products and titanium metal powder was divided into equal five parts to make block samples. Each part (13.21 g) of the powder mixture was hot pressed at 1200°C and 29 MPa for 2 h using a graphite die in a stream of nitrogen gas. A hot-pressing cycle was the same as in the previous study[3] except three samples (S90003 to S90005) were cooled to 300°C in 3 h and then naturally cooled to the room temperature. Another sample (S90002) was hot pressed for 1 h at the same condition and then naturally cooled to the room temperature because of break down of a thermocouple for a power controller[3] during hot pressing.

Density Measurement

Peripheries of block samples were polished up to No. 600 with grid abrasive paper, and their flat faces were finished with 6 μm diamond paste. The densities of 2-cm-dia. × 1-cm-high cylinders were measured by the water displacement method. The water was kept at 30°C.

RESULTS AND DISCUSSION

Activity

The curium source of 1.579 g was incorporated in 67.38 g of the solidified sample. Activity of the curium source was obtained through decay correction of mass assay from ORNL. On 28 February, 1990, the 1.579 g of the curium source has 1.846 TBq (49.90 Ci) of ^{244}Cm activity and 1.854 TBq (50.10 Ci) of total alpha activity. This leads to specific ^{244}Cm activity and specific alpha activity of 27.4 and 27.5 GBq·g^{-1} (0.741 and 0.744 Ci·g^{-1}), respectively.

Density

Figure 1 shows dependence of densities of the polished block samples (S90002 and S90005) upon the cumulative alpha decays up to a dose of 12.4×10^{17} alpha decays·g^{-1}. If the densities are assumed to decrease in a parallel manner with an exponential relation obtained from the curium-doped JW-A titanate ceramic (see Eq.(1) in Ref. 4), the least-squares method on the data shows that the S90002 and S90005 densities were higher than that of the curium-doped JW-A sample by 0.0457 and 0.0542 g·cm^{-3}, respectively. This results in the initial and saturated

densities of 4.3526 and 3.8871 $g \cdot cm^{-3}$ for the sample S90002, and those of 4.3611 and 3.8956 $g \cdot cm^{-3}$ for the sample S90005, respectively. These values imply that the saturated increments of the densities of curium-doped sodium-free titanate ceramic could also reach similar high values to that of the sodium-bearing titanate nuclear waste form (~10%)[4].

In Fig. 1, the PW-4b samples give no extra decrease unlike the JW-A sample, up to a dose of 12.4×10^{17} alpha decays$\cdot g^{-1}$. At this alpha-decay dose, the increment of densities of the curium-doped PW-4b samples was -1.7%, while that of the curium-doped JW-A sample had been -2.3% although it was also expected to have been -1.7%[2],[4]. This means that cracking due to volume swelling did not still affect density change of the PW-4b samples. This also implies that fragility of the sodium-free samples was lower than that of the sodium-bearing sample. Leach test on the curium-doped sodium-free titanate ceramic is now being carried out to examine its chemical durability.

REFERENCES

(1) A.E. Ringwood, S.E. Kesson, K.D. Reeve, D.M. Levins and E.J. Ramm: "Synroc"; pp. 233-334 in Radioactive Waste Forms for the Future. Edited by W. Lutze and R.C. Ewing. Elsevier Science Publishing Company Inc., New York, NY, 1988.

(2) H. Mitamura, S. Matsumoto, K.P. Hart, T. Miyazaki, E.R. Vance, Y. Tamura, Y. Togashi and T.J. White: "Aging Effects on Curium-Doped Titanate Ceramic Containing Sodium-Bearing High-Level Nuclear Waste"; To be published in J. Am. Ceram. Soc.

(3) H. Mitamura, S. Matsumoto, W.J. Buykx and S. Tashiro: "Fabrication of Curium-Doped SYNROC for an Alpha Radiation Stability Test", Nucl. Technol., 85, 109-17 (1989).

(4) H. Mitamura, S. Matsumoto, T. Miyazaki, T.J. White, K. Nukaga, Y. Togashi, T. Sagawa, S. Tashiro, D.M. Levins and A. Kikuchi: "Self-Irradiation Damage of a Curium-Doped Titanate Ceramic Containing Sodium-Rich High-Level Nuclear Waste", J. Am. Ceram. Soc., 73[11] 3433-41 (1990).

Table 1 Comparison of nominal composition of curium-doped titanate ceramics containing PW-4b and JW-A high-level nuclear waste

Element	Content (Wt%)	
	PW-4b	JW-A
[Precursor]		
TiO_2	62.03	62.24
CaO	9.67	9.70
ZrO_2	5.92	5.95
BaO	4.79	4.81
Al_2O_3	4.70	4.72
[Oxygen getter]		
Ti(metal)	1.98	1.99
[Simulated HLW]		
SeO_2	-	0.011
Rb_2O	-	0.064
SrO	0.275	0.176
Y_2O_3	0.157	0.104
ZrO_2	1.246	0.852
MoO_3	1.304	0.899
MnO_2	-	0.133
RuO_2	0.791	0.506
Rh_2O_3	0.150	0.105
PdO	0.379	0.276
Ag_2O	0.021	0.015
CdO	0.032	0.016
SnO_2	-	0.010
Sb_2O_3	-	0.002
TeO_2	0.155	0.118
Cs_2O	0.918	0.507
BaO	0.416	0.325
La_2O_3	-	0.263
CeO_2	1.246	0.524
Pr_6O_{11}	-	0.257
Nd_2O_3	0.752	0.237
$CmO_2 + PuO_2$	2.344	1.614
Na_2O	-	1.652
P_2O_5	0.179	0.167
Fe_2O_3	0.403	1.382
Cr_2O_3	0.092	0.200
NiO	0.037	0.175

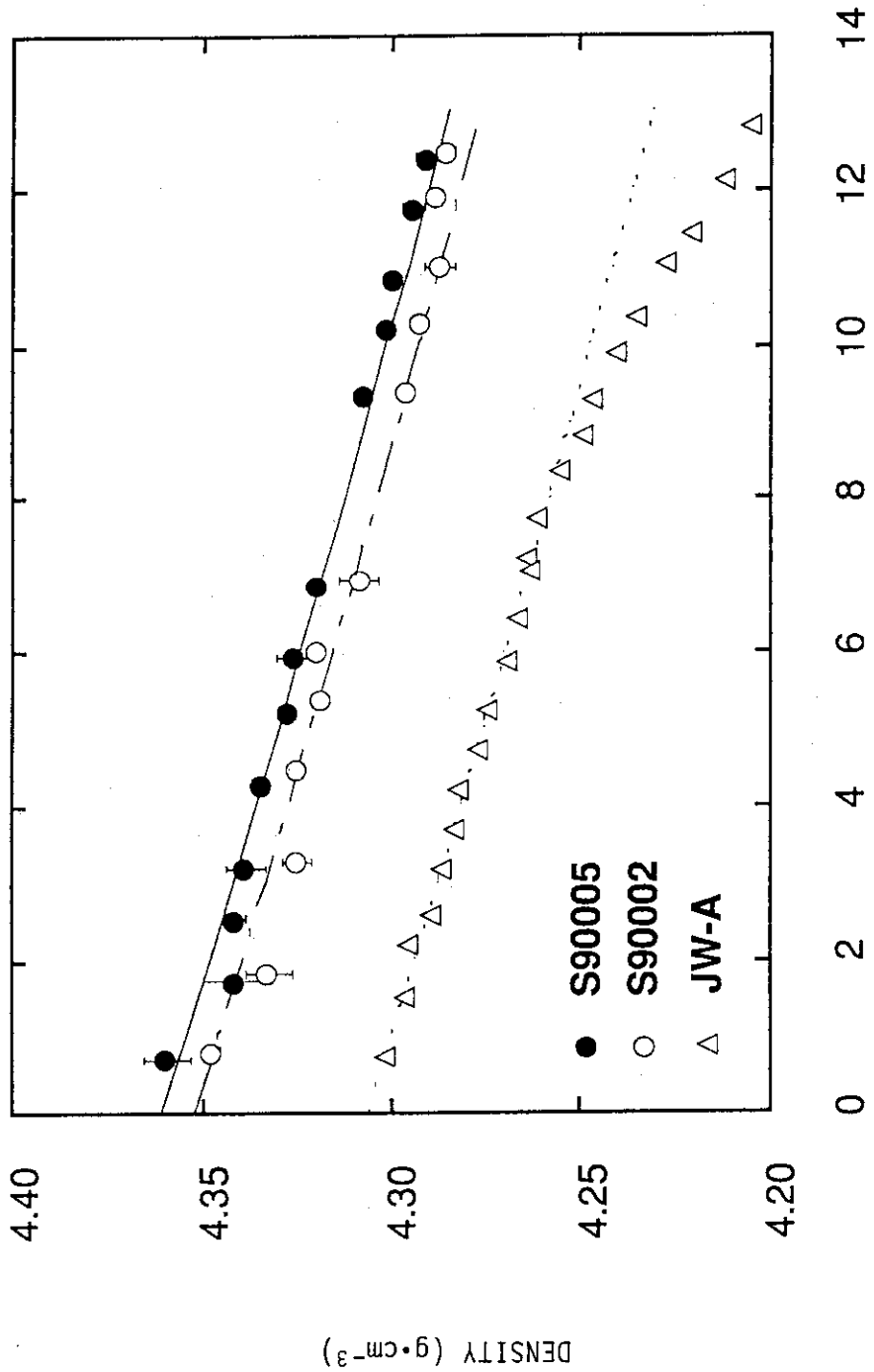

Fig. 1 Density of curium-doped titanate ceramics versus alpha-decay dose. Fitted curves for the sodium-free samples (S90005 and S90002) were derived from fitting under the assumption that their densities varied in concert with change in density of the sodium-bearing sample (JW-A).

1.2.2 Solubility of Simulated HLW Elements in Pyrochlore Structure

I. Hayakawa and H. Kamizono

INTRODUCTION

We have found that lanthanum zirconate($La_2Zr_2O_7$) with a pyrochlore structure can be used as a superior host phase for actinide and lanthanide elements in high-level nuclear waste. The solubility of Ce, Nd and Sr in $La_2Zr_2O_7$ is determined because the elements may simulate the segregation of actinide and lanthanide elements at the grain boundaries of polycrystalline $La_2Zr_2O_7$. The results show that $La_2Zr_2O_7$ is a promising material for confining actinide and lanthanide elements in its crystal structure.

EXPERIMENTAL

The system $La_2Zr_2O_7$-$Nd_2Zr_2O_7$ was examined to clarify the solubility limit of Nd into $La_2Zr_2O_7$. The solution of Nd needs the addition of stoichiometric Zr atoms, and therefore $Nd_2Zr_2O_7$ was used as an end member of the system.

The solution of Ce also needs the addition of stoichiometric Zr atoms. However, the stable form of Ce ion in air is Ce^{4+} and $Ce_2Zr_2O_7$ is not a stable compound in air. So we used 2 CeO_2•2 ZrO_2 rather than $Ce_2Zr_2O_7$ as an end member to examine the solubility of Ce and we examined the systems $La_2Zr_2O_7$-2 CeO_2•2 ZrO_2.

It is expected that Sr will be confined in the La site of $La_2Zr_2O_7$, judging from its ionic radius, and the presence of Ce^{4+} ions may promote the solution of Sr into $La_2Zr_2O_7$ because a pair of Sr^{2+} and Ce^{4+} can easily substitute the La sites in $La_2Zr_2O_7$. So the composition 2(SrO• CeO_2•2 ZrO_2) was taken as an end member to equalize the ratio of La to Ce.

The nitrates of La, Zr, Nd, Ce and Sr were mixed and dissolved in 0.5 M HNO_3 solution and calcined at 700°C in air. Calcined powders are formed to the pellets. The pellets were fired at 1400°C for 16 h in air and ground in an Al_2O_3 mortar. The ground powder was again pressed into pellets and fired at 1400°C for 16 h in air to homogenize the chemical composition and to complete the reation. The fired pellets were

ground to powder and subjected to X ray analysis.

RESULTS AND DISCUSSION

The system $La_2Zr_2O_7$-$Nd_2Zr_2O_7$

Figure 1 shows the change of lattice parameter in the system $La_2Zr_2O_7$ -$Nd_2Zr_2O_7$. The crystal phase in this system has a pyrochlore structure. The lattice parameter of the pyrochlore phase decreases with the increase of Nd linearly. This means that Nd tends to be substituted for La in the solid solution, because the ionic radius of Nd is smaller than that of La and is larger than that of Zr.

The system $La_2Zr_2O_7$-2 CeO_2•2 ZrO_2

The lattice parameter in the system $La_2Zr_2O_7$-2 CeO_2•2 ZrO_2 is shown in Fig. 2. The lattice parameter of the pyrochlore phase decreases with the increase of 2 CeO_2•2 ZrO_2 up to 27 mol%, then becomes constant with the formation of a fluorite phase. Hence, the solubility limit of Ce was estimated to be 27 mol%. The decrease of the lattice parameter can be explained by the small ionic radius of Ce compared with that of La. The lattice parameter of the fluorite phase increases above 80 mol% of 2 CeO_2• 2 ZrO_2. This is because, as seen in Fig. 3, tetragonal ZrO_2 occurs above 60 mol% of 2 CeO_2•2 ZrO_2, resulting in the increase of ZrO_2 in a fluorite structure above 80 mol% of 2 CeO_2•2 ZrO_2.

At the composition of 2 CeO_2•2 ZrO_2, 30% of the tetragonal ZrO_2 and 70% of the fluorite phase occur (Fig. 3). The phase diagram for ZrO_2-CeO_2 indicates that the volume ratio of fluorite to tetragonal ZrO_2 is 70:30 at the molar ratio of 50 CeO_2:50 ZrO_2, when it is calculated from the lattice parameters and the molar ratio of fluorite and pyrochlore phases[1]. This is in line with the present results.

The system $La_2Zr_2O_7$-2(SrO•CeO_2•2 ZrO_2)

Figure 4 shows the lattice parameters in the system $La_2Zr_2O_7$-2(SrO• CeO_2•2 ZrO_2). The broken line shows the lattice parameters of the pyrochlore structure in the system $La_2Zr_2O_7$-2 CeO_2•2 ZrO_2. The lattice parameter of the pyrochlore phase increases with the increase of Sr up to 2.5 mol% and then decreases. A fluorite phase occurs at the composition of 67 mol% of 2(SrO•CeO_2•2 ZrO_2). The lattice parameters of the fluorite

phase are on the line extrapolated from the values of the pyrochlore phase. The composition of the crystal phases in the system $La_2Zr_2O_7$-$2(SrO{\cdot}CeO_2{\cdot}2\ ZrO_2)$ is shown in Fig. 5. In this figure, $SrTiO_3$ occurs when Sr is added more than 5 mol% and the quantity of $SrZrO_3$ increases with the increase of Sr. Therefore, the solubility limit of Sr with the co-existence of Ce is estimated to be less than 5 mol%. If the increase of the lattice parameter is due to the solution of Sr into $La_2Zr_2O_7$, then the solubility limit of Sr is expected to be about 2.5 mol%. This value is large in contrast to the solubility limit of Sr in a fluorite structure, 0.3%[2]. Wakiya et al. has reported that $(Sr,Ce)_2Zr_2O_7$ is not a stable compound[3], and this may be one of the reasons why Sr is not easily confined in the pyrochlore structure.

The lattice parameters of the pyrochlore structure were greater than those in the system $La_2Zr_2O_7$-$2\ CeO_2{\cdot}2\ ZrO_2$. There are two reasons: first, the solid solution of Sr with a larger ionic radius than La makes the lattice parameter of the pyrochlore structure increase, and second, the solid solution content of Ce in a pyrochlore phase decreases because of the solution of Ce into $SrZrO_3$.

Note that Fig. 4 shows that the solubility limit of Ce in this system is wider than that in the system $La_2Zr_2O_7$-$2\ CeO_2{\cdot}2\ ZrO_2$. This is because Sr with a larger ionic radius than La facilitates the solution of Ce into $La_2Zr_2O_7$.

REFERENCES

(1) P. Duran, M. Gonzalez, C. Moure, J.R. Jurado and C. Pascual: J. Mater. Sci. 25, 5001 (1990).

(2) T. Muromura and Y. Hinatsu: J. Nucl. Mater. 151, 55 (1987).

(3) N. Wakiya, N. Kieda et al., in the Japan Ceramic Society Annual Meeting, proceeding, (Jap. Ceram. Soc., Japan. 1991), p.222.

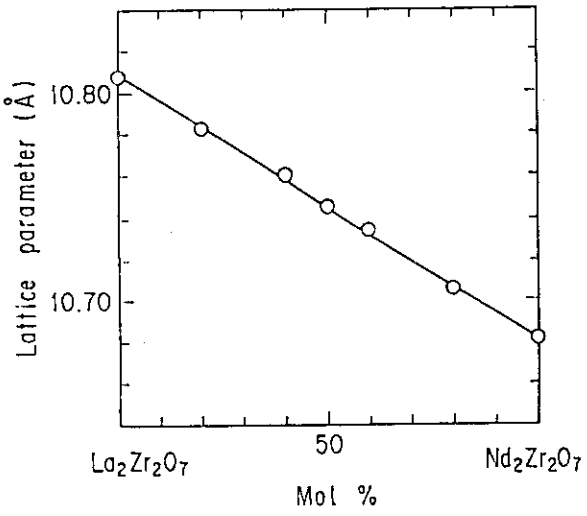

Fig. 1 Lattice parameter in the system $La_2Zr_2O_7$-$Nd_2Zr_2O_7$

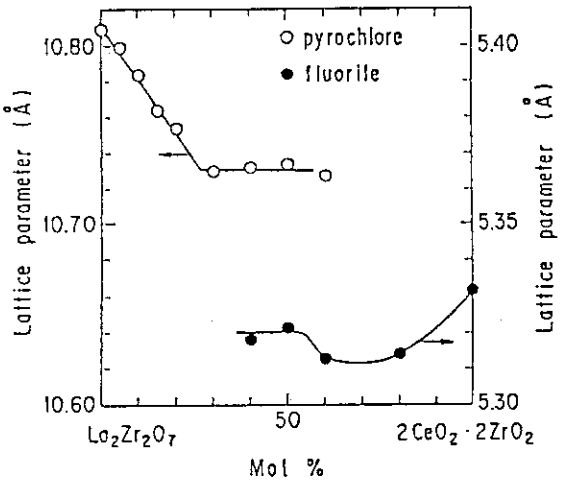

Fig. 2 Lattice parameter in the system $La_2Zr_2O_7$-2 CeO_2・2 ZrO_2

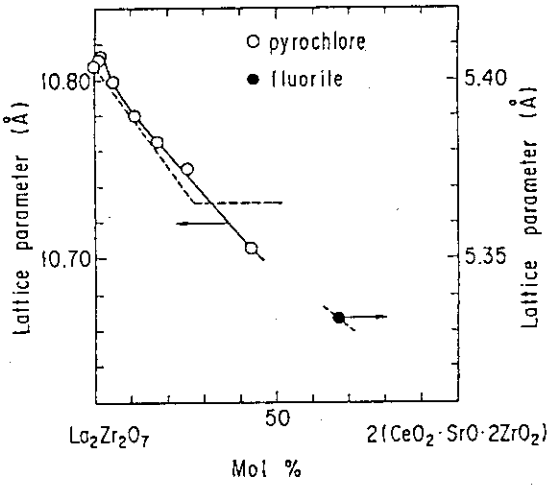

Fig. 4 Lattice parameter in the system $La_2Zr_2O_7$-2(SrO・CeO_2・2 ZrO_2)

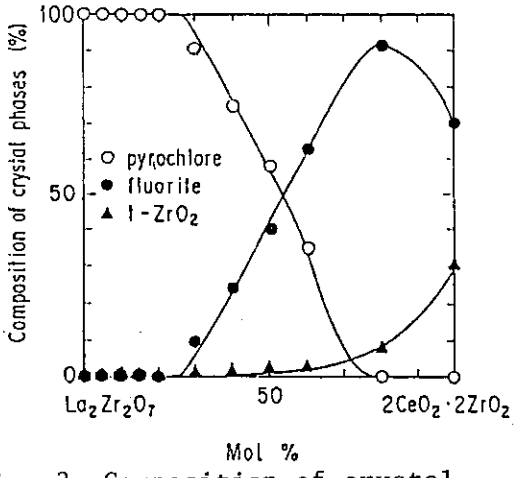

Fig. 3 Composition of crystal phases in the system $La_2Zr_2O_7$-2 CeO_2・2 ZrO_2

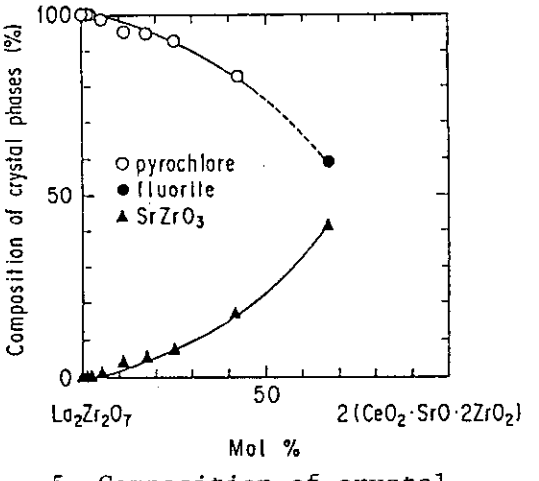

Fig. 5 Composition of crystal phases in the system $La_2Zr_2O_7$-2(SrO・CeO_2・2 ZrO_2)

1.3 Performance of Engineered Barrier Materials

1.3.1 Corrosion Test of Stainless Steel under Gamma Rays Irradiation

K. Osada

INTRODUCTION

Gamma rays, generated from fission products in high-level radioactive waste, are considered to change the environment around the canister and overpack container. The radiolysis of water is occurred by gamma rays, therefore, $H\cdot$, $OH\cdot$, e^-_{aq}, H_2O_2 and H_2 are produced, which are considered to affect these metals' corrosivity. The measurements of oxidation-reduction potential and corrosion potential of stainless steel have been conducted to examine the effect of gamma rays irradiation. The pitting potential has also been measured to examine the pitting corrosivity.

EXPERIMENTAL

The oxidation-reduction potential and corrosion potential of stainless steel have been measured in the NaCl solutions under gamma rays irradiation by using electrochemical method. Platinum was used in measuring the oxidation-reduction potential of NaCl solution. The specimens of type SS-304 of 1 cm × 1 cm in size were used, the chemical composition of type SS-304 is shown in Table 1. The measurements were conducted in the NaCl solutions of 1M, 0.1M and 0.01M. Cobalt 60 was used as the source of gamma rays at the dose rates of 1×10^6, 1×10^5 and 1×10^4 R/h. This experiment was conducted at 30°C and 60°C. All these solutions were bubbled by Ar gas to remove resolved O_2. The scan rate was 100 mV/min in measuring the pitting potential.

RESULTS AND DISCUSSION

The changes of oxidation-reduction potential are shown in Fig. 1 in the NaCl solutions under the irradition of gamma rays at the dose rate of 1×10^6 R/h at 30°C. In the 1M NaCl solution, before the irradiation, the oxidation-reduction potential was 180 mV (vs. SCE). During the ir-

radiation, the potential was -300 mV by the formation of H_2. After the irradiation was finished, the potential increased to near 100 mV again. In the 0.1M and 0.01M NaCl solutions, however, during the irradiation, the potentials were -500 mV. Consequently, it is concluded that the 0.1M and 0.01M NaCl solutions contain much H_2 in comparison with the 1M NaCl solution.

The changes of corrosion potential of stainless steel are shown in Fig. 2 in the NaCl solutions under the irradiation of gamma rays at the dose rate of 1×10^6 R/h at 30°C. In the 1M NaCl solution, the corrosion potential of stainless steel increased from -660 mV to 50 mV during the 3 hours irradiation. In the 0.1M and 0.01M NaCl solutions, however, the corrosion potentials increased to only -100 mV during the 6 hours irradia tion. Consequently, it is concluded that the 1M NaCl solution contains much H_2O_2 or O_2 in comparison with the 0.1M and 0.01M NaCl solutions, and that the oxidizability of 1M NaCl solution is stronger than those of 0.1M and 0.01M NaCl solutions. The changes of corrosion potential of stainles steel are shown in Fig. 3 in the 1M NaCl solution under the irradiation of gamma rays at the dose rates of 1×10^6, 1×10^5 and 1×10^4 R/h at 30°C. The corrosion rate increased by increasing of dose rate. The solution at the dose rate of 1×10^4 R/h was almost the same as the solution without irradiation.

The measurements of pitting potential of stainless steel are shown in Fig. 4 in the 1M NaCl solution under the irradiation of gamma rays at the dose rate of 1×10^6 R/h. The pitting potentials were 150 mV at 30°C and 50 mV at 60°C. The measurements of pitting potential of stainless steel are shown in Fig. 5 in the 0.1M NaCl solution under the irradiation of gamma rays at the dose rate of 1×10^6 R/h. The pitting potentials were 300 mV at 30°C and 200 mV at 60°C. In the 1M NaCl solution under the irradiation of gamma rays, the corrosion potential of stainless steel was 50 mV, and the pitting potential of stainless steel was 50 mV at 60°C. The corrosion potential was, therefore, more than the pitting potential, and the pitting corrosion is considered to be occurred in the 1M NaCl solution under the irradiation of gamma rays at the dose rate of 1×10^6 R/h at 60°C.

Table 1 Chemical composition of type SS-304

	C	Si	Mn	P	S	Ni	Cr
%	0.075	0.52	0.95	0.010	0.024	9.2	18.22

* Balance: Fe

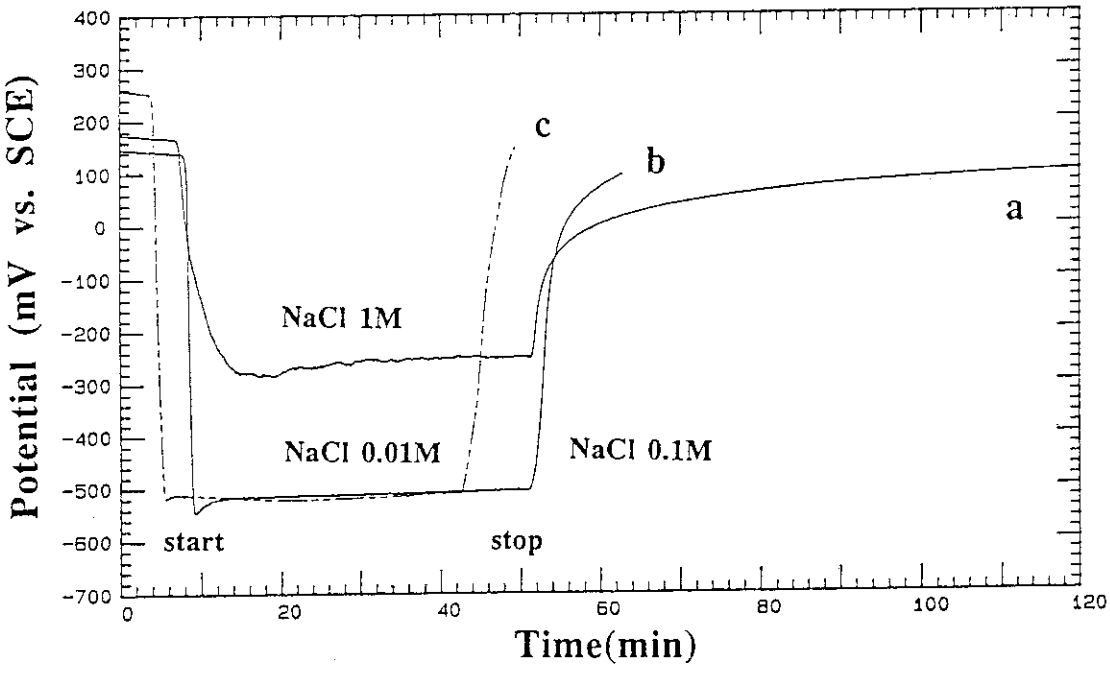

Fig. 1 Oxidation-reduction potentials in the NaCl solutions of 1M(a), 0.1M(b) and 0.01M(c) under the irradiation of gamma rays at the dose rate of 1×10^6 R/h at 30°C.

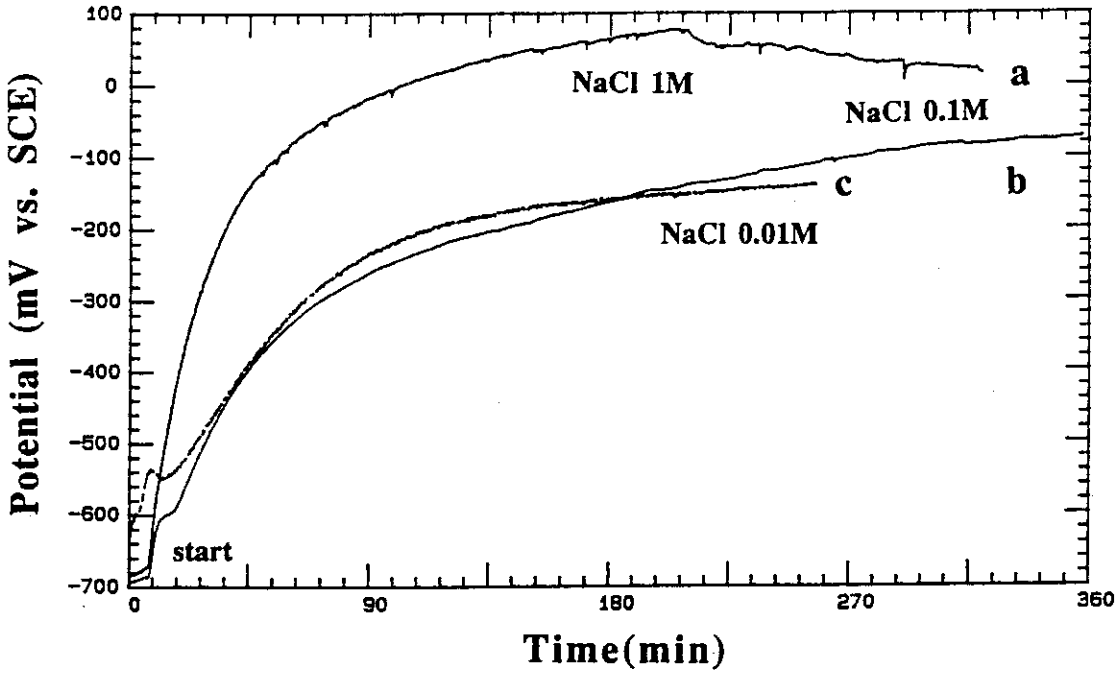

Fig. 2 Corrosion potentials of stainless steel in the NaCl solutions of 1M(a), 0.1M(b) and 0.01M(c) under the irradiation of gamma rays at the dose rate of 1×10^{6} R/h at 30°C.

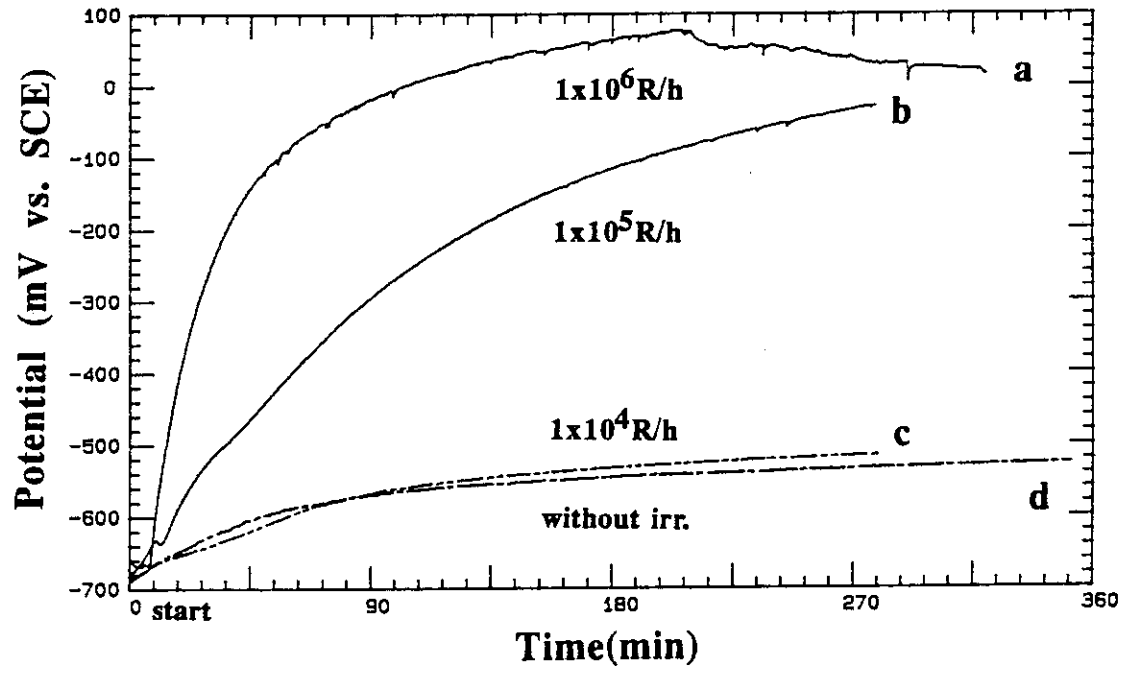

Fig. 3 Corrosion potentials of stainless steel in the 1M NaCl solution under the irradiation of gamma rays at the dose rates of 1×10^{6}(a), 1×10^{5}(b) and 1×10^{4}(c) R/h and under without irradiation(d) at 30°C.

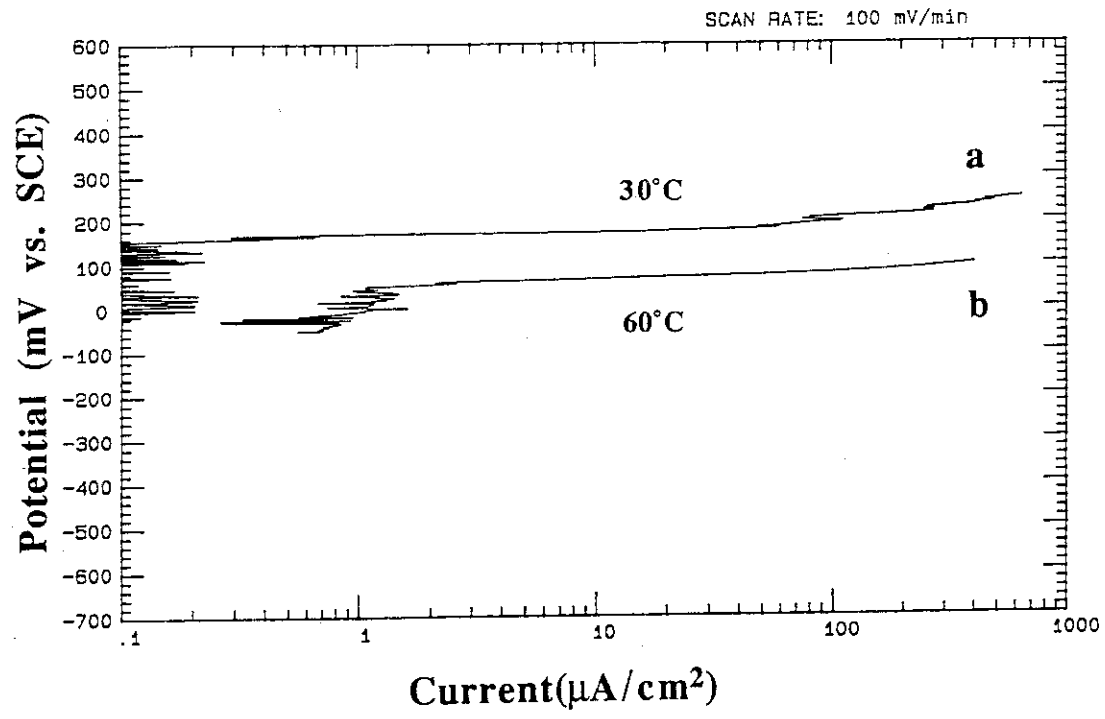

Fig. 4 Pitting potentials of stainless steel in the 1M NaCl solutions under the irradiation of gamma rays at the dose rate of 1×10^6 R/h at 30°C(a) and 60°C(b).

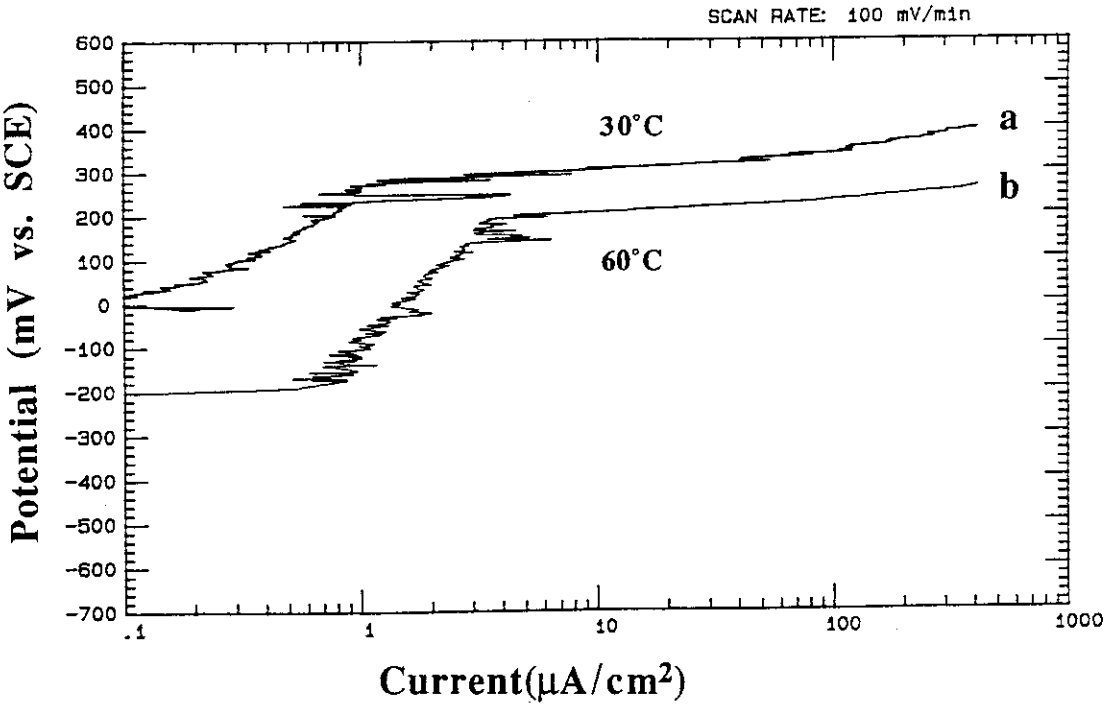

Fig. 5 Pitting potentials of stainless steel in the 0.1M NaCl solutions under the irradiation of gamma rays at the dose rate of 1×10^6 R/h at 30°C(a) and 60°C(b).

1.3.2 Sorption Characteristics of Neptunium on Smectite

N. Kozai

INTRODUCTION

The use of bentonite as a buffer materials in radioactive waste disposal is based on its properties of low permeability and of large cation exchange capacity. Sorption characteristics of neptunium on smectite which is one of the major clay minerals contained in bentonite (buffer material) have been studied by batch experiments.

EXPERIMENTAL

Sorption experiments were carried out to discuss the relationship between pH of the neptunium solution and the amount of neptunium adsorbed on smectite. Smectite was added to the neptunium solution in polycarbonate centrifugation tube after the pH adjustment, and the mixture was kept at 20°C for 10 days. After the adsorption experiment, the phase separation was carried out by centrifugation at 12000 rpm for 1 hr, and the pH and concentration of neptunium of the supernatant were measured.

Subsequently, desorption experiments using the sequential extraction procedure were carried out to clarify the association of neptunium with smectite. The smectite on which neptunium was adsorbed was firstly treated with a 1 M KCl and secondary a 1 M HCl solution at 20°C for 2 days. At the end of each extraction step, the suspended solution was separated by the centrifugation mentioned above, and concentration of the extracted neptunium was measured. Finally, concentrations of the residual neptunium in the solid phases were measured after the residues were dissolved by a HF solution with heating.

RESULTS

The Kd values of neptunium for smectite are shown in Fig. 1 as a function of pH of the solution. The highest Kd values appeared around pH 2, then decreased abruptly with increasing pH, and then became con-

stant in the pH region from 5 to 10 and increased with increasing pH above 10. It is known that Kd values of neptunium for bentonite became constant in the acidic and neutral region, and then increased with the increase of pH in the alkaline solution[1]. These results are the same as those obtained for bentonite above pH 5, but are considerably different in the lower pH region.

Percent fractions of neptunium desorbed from smectite are shown in Fig. 2. In all of the pH region, the neptunium adsorbed on smectite was entirely desorbed with a 1 M KCl and a 1 M HCl solutions. However, there are two different associations of neptunium with regard to the pH of the solutions. One is the desorbable association with a 1 M KCl solution observed at neutral and alkaline solution. The other is the undesorbable association with a 1 M KCl solution observed at low pH solution.

REFERENCE

(1) Sakamoto et al.: "Adsorption Behavior of Neptunium for Soil", Radioactive Waste Management and the Nuclear Fuel Cycle, 15, 13, 1990.

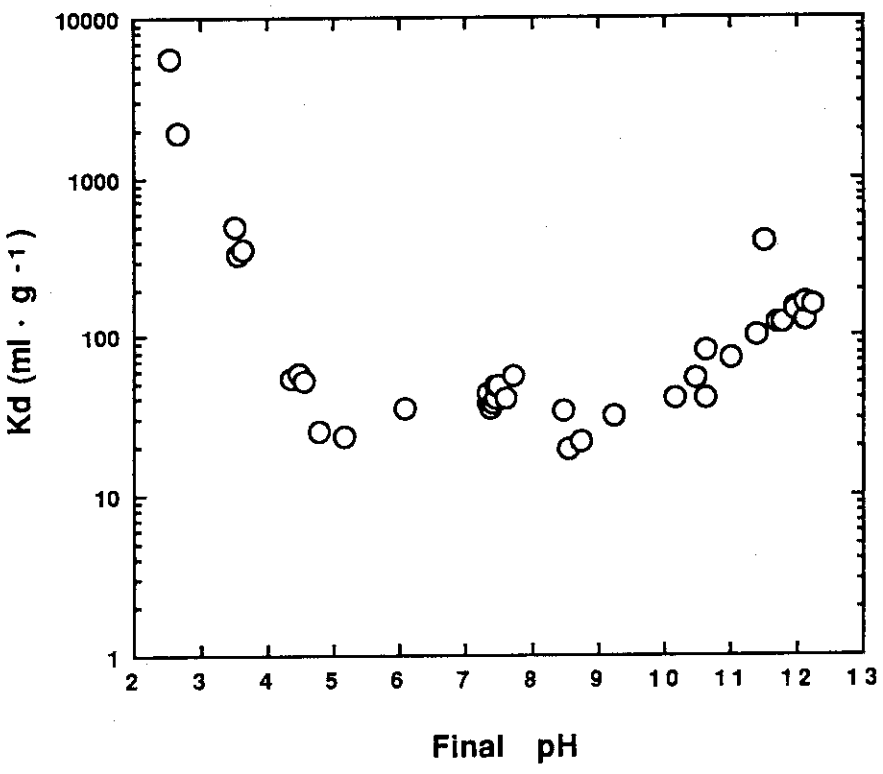

Fig. 1 The pH dependence of Kd values for Na-smectite

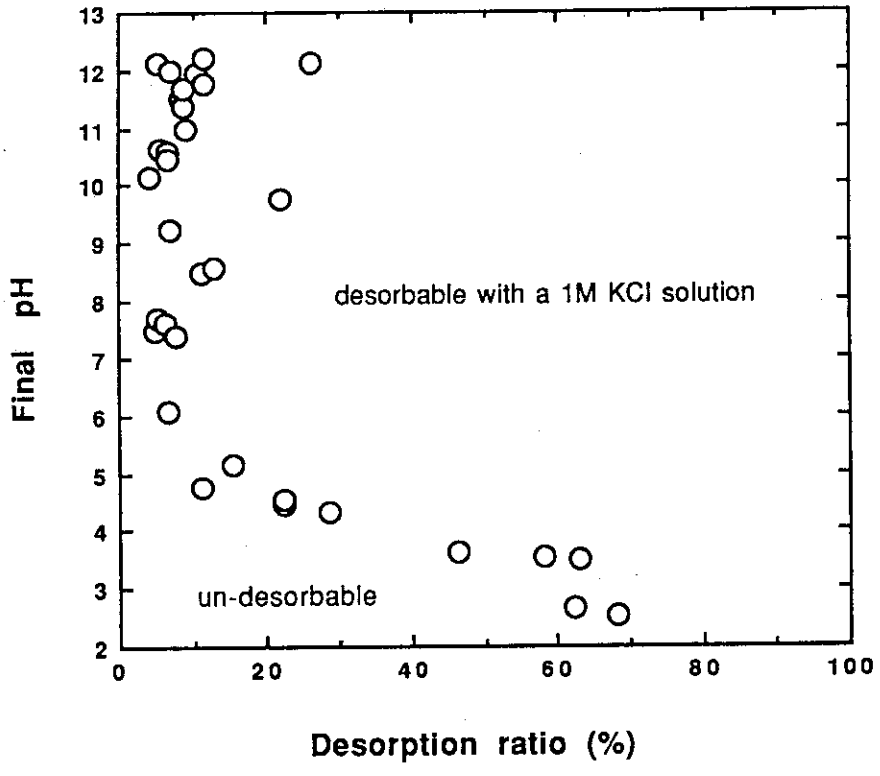

Fig. 2 Percent fractions of neptunium desorbed from Na-smectite

2. Safety Evaluation Study for Geological Disposal

2.1 Chemical Behavior of Radionuclides in Water

2.1.1 Solid-liquid Equilibrium of Neptunium(V) under Exclusion of CO_2[1]

Hiroshi ITAGAKI[2], Shinichi NAKAYAMA[3], Satoru TANAKA[2]
Muneaki SENOO[3] and Michio YAMAWAKI[2]

ABSTRACT

The effect of ionic strength on the solubility of neptunium(V) hydroxide was studied under the oxidizing, CO_2-free argon atmosphere in the pH range of 7 to 12.5 at room temperature (20-25°C). The solubility was mainly approached from oversaturation direction. The ionic strength was adjusted by $NaClO_4$ to 0.012, 0.10, 0.40 or 0.80.

Solid-liquid equilibria were attained in one to two months, depending on pH and ionic strength. From the pH-dependent solubility curves, the solubility product (K_{sp}), and the first and the second hydrolysis constants (β_1,β_2) were estimated:

$\log K_{sp}=-10.9\pm0.06$, $\log\beta_1=4.3\pm0.6$ at I=0.80,
$\log K_{sp}=-9.78\pm0.08$, $\log\beta_1=3.4\pm0.2$, $\log\beta_2=5.5\pm0.3$ at I=0.40,
$\log K_{sp}=-9.25\pm0.02$, $\log\beta_1=3.3\pm0.4$, $\log\beta_2=6.1\pm0.7$ at I=0.10 and
$\log K_{sp}=-8.1\pm0.1$, $\log\beta_1=3\pm1$ at I=0.012,

where I is the ionic strength.

Neptunium hydroxide precipitates showed no X-ray diffraction peaks from 1 day to 3 months after preparation. This result indicates that the precipitates remained non-crystalline for up to 3 months.

---

1 This article is a part of the study entitled "Effect of ionic strength on the solubility of neptunium(V) hydroxide", which was presented at the third international conference on chemistry and migration behavior of actinides and fission products in the geosphere (Jerez de la Frontera, Spain, October 14-18, 1991) and accepted to Radiochimica Acta.

2 Nuclear Engineering Research Laboratory, University of Tokyo, Tokai, Ibaraki 319-11, Japan

3 Japan Atomic Energy Research Institute, Tokai, Ibaraki, 319-11, Japan

INTRODUCTION

Hydrolysis, as well as redox reaction and carbonate complexation, is one of critical reactions controlling the chemical behavior of neptunium in near-neutral aqueous solutions[1]. Reliable data on the solubility and hydrolysis constants are, therefore, needed to predict the concentrations in natural waters.

The hydrolysis of neptunium(V) and the solubility of the hydroxide, NpO OH, have been studied by several researchers, and many sets of solubility product and hydrolysis constants have been obtained as listed in Table 1[2-12]. However, the data have not yet systematically understood because of different experimental conditions employed such as ionic strength and temperature. Sometimes the data are doubtful due to large uncertainties arising from only a limited number of experimental points, and/or from poorly-controlled experimental conditions.

Speciation of the solubility-controlling solid is also essential to the solubility determination. Solubility depends strongly on the state of the solid phase. Crystallization can change the solubility, as observed by Strickert et al.[13] for neptunium(IV) hydrous oxide.

In the present study, the hydrolysis of neptunium(V) was studied under the oxidizing condition in the pH range of 7 to 12.5. The objective is to obtain the dependence of the solubility product and the hydrolysis constants on the ionic strength of the solutions. Attempt was made to determine the state of the solubility-controlling solid phase.

EXPERIMENTAL

(Reagents)

A neptunium-237 (^{237}Np) stock solution was prepared from neptunium dioxide powder (NpO_2, >99 wt%, CEN, Fontenay aux Roses, France). The powder was dissolved in concentrated HNO_3, fumed to near dryness, and the residual was dissolved in 1M $HClO_4$. The neptunium concentration of the final stock solution was 1×10^{-1} M.

Deionized water used in the experiments was deaerated by boiling. An NaOH solution for pH adjustment was prepared from reagent-grade pellets of NaOH and the deaerated deionized water. In order to avoid carbonate contamination, carbonate contained in the NaOH solution was

removed by adding $BaCl_2$ through $BaCO_3$ precipitation[14]. This solution was placed under an inert atmosphere (>99.995% Ar) in a glove box.

(Procedure)

All experiments were conducted in a glove box under an Ar (>99.995%) atmosphere at room temperature (20-25%). The Ar gas was passed through a $BaCl_2$ solution before introduction into the glove box to ensure the removal of CO_2. The $BaCl_2$ solution was also placed in the glove box. The inner pressure of the glove box was kept 5 to 10% higher than the outer pressure to prevent air intrusion.

Neptunium sample solutions were prepared in 20 ml glass vials. The initial concentrations were between 10^{-2} M and 10^{-3} M. The pH of the solutions were adjusted by NaOH and $HClO_4$. The solubility measurement was mainly approached from oversaturation direction. The oversaturation direction consisted of adding an excess amount of neptunium from the stock solution to $NaClO_4$ solution and monitoring the concentration of neptunium until equilibrium was reached. A few samples were approached from undersaturation direction. In the undersaturation direction, precipitates formed in the oversaturation direction were separated within one day after the preparation and dissolved in fresh $NaClO_4$ solution. The ionic strength (I) of the $NaClO_4$ solution was 0.012, 0.10, 0.40 or 0.80.

Aliquots of the supernatant (usually 0.2 ml) were drawn from the sample solutions and filtered through a Millipore 10,000 molecular weight cutoff filter to separate solids from solutions. Loss of neptunium by sorbing on the filter is negligible[15]. Fifty microliters of the filtrate were dried on cleaned stainless steel planchettes. The α-radioactivity was measured with a 2π gas flow proportional counter. The filtrates from solutions of ionic strength of 0.40 and 0.80 were diluted before drying to avoid the dried salts, which inhibits exact counting of α-radioactivity. Some of the separated solids were subject to X-ray diffractometry to examine the crystallization.

RESULTS AND DISCUSSION

Attainment of equilibrium was confirmed for some selected sample solutions by measuring the concentrations of neptunium at intervals of

time. The neptunium concentrations measured in the course of equilibration are shown in Fig. 1. The concentrations in higher-pH solutions (pH 11) approach the steady-state values a little more slowly than those in lower-pH solutions (pH 9). Steady-state concentrations were found to be attained within between 1 and 3 months for all values of pH and ionic strength.

X-ray diffractometric analysis was made for precipitated solids separated from several sample solutions. No X-ray peaks were observed in any of the precipitates stored for 1 day to 3 months after the sample preparation. This result indicates that the precipitated hydroxide remained non-crystalline for three months.

The obtained solubility values are plotted in Fig. 2 as a function of pH. We found the solubility curves consisting of two parts. One is concave-type dependence observed at the higher pH region. This pH dependence typically represents the hydrolytic behavior of neptunium(V) [8,10,12]. On the other hand, a pH-independent part appeared at the lower pH region. The pH region depends on the ionic strength such as 7.5 to 9 for I=0.012 and 6 to 8.5 for I=0.10. This constant solubility is the unexpected result which we cannot predict from previous knowledge about the hydrolytic behavior of neptunium(V) [8,10,12].

We estimate the solubility product K_{sp}, and the first and the second hydrolysis constants β_1 and β_2 from the data of the pH-dependent part of the solubility curves. The hydrolysis reactions of neptunium(V) are expressed by

$$NpO_2^+ + OH^- = NpO_2OH \qquad (1)$$

and

$$NpO_2OH + OH^- = NpO_2(OH)_2^-. \qquad (2)$$

The total concentration of neptunium(V), $[Np(V)]_T$, in solution is given by

$$[Np(V)]_T = [NpO_2^+]+[NpO_2OH]+[NpO_2(OH)_2^-] \qquad (3)$$

or

$$[Np(V)]_T = K_{sp}/[OH^-]+K_{sp}\beta_1+K_{sp}\beta_2[OH^-] , \qquad (4)$$

where

$$K_{sp} = [NpO_2^+][OH^-] \qquad (5)$$

$$\beta_i = [NpO_2(OH)_i^{1-i}]/[NpO_2^+][OH^-]^i. \qquad (6)$$

Weighed non-linear regressions of the experimental data to eq.(4) gives the values of K_{sp}, β_1 and β_2 for each ionic strength. The obtained values are listed in Table 2. In the case of I=0.012, β_1 and β_2 are not listed because of the large uncertainties derived.

The dependence of K_{sp}, β_1 and β_2 on the ionic strength and the values for infinite dilution (I=0) can be predicted by the specific ion interaction theory[16]. The Nuclear Energy Agency (NEA) of the Organization of Economic Cooperation and Development (OECD) uses this method for their Thermochemical Data Base project[17], and has published guidelines on the application of this method[18]. At present the solubility products and hydrolysis constants we obtained are not exact enough to be applied to the theory. We will add some more experimental points, particularly at higher pH regions, to obtain more exact and reliable constants.

We have obtained pH-independent, constant solubilities. The phenomenon has not been reported previously. There are only a few researchers who showed the solubility curves as a function of pH. Lierse et al.[8] measured the solubility in 1M $NaClO_4$ solutions at pHs between 6.8 and 13. They did not observe the constant solubility values in this pH region. Nakayama et al.[10] studied at pHs of 7 to 13 in 0.01M $NaNO_3$ solutions, but they did not report such tendency. Solubility curves recently obtained by Neck et al.[12] for 0.1M and 1.0M $NaClO_4$ solutions also do not show the tendency, while the curve for 3.0M $NaClO_4$ solution represents some constant values, though not so clear, at pH between 7 and 8. In the present results, the constant solubility region appears at lower pHs in solutions of higher ionic strength. The occurrence of the constant solubility seems related to the ionic strength to the solutions.

Analyses were made to identify the precipitates under the above pH regions and aqueous species in contact with them. First, the solids were analyzed by X-ray diffractometry. No peaks were observed; accordingly it was concluded that no crystalline materials developed. A spectrophotometric analysis shows that neptunium in the strong brown solutions in contact with the precipitates was pentavalent. The filtration test was also made for neptunium in solution. Concentrations of neptunium were not different between the unfiltered supernatant and the filtrate, meaning that no colloidal substances existed. At pH lower than 3, no precipitates were formed, i.e., the solubility is probably much higher than those constant values. At present we have not yet found any reasonable explanations for the pH-independent solubility values.

ACKNOWLEDGEMENTS

We thank Dr. T. Kimura for his spectrophotometric work.

REFERENCES

(1) Kim, J.I., Handbook on the Physics and Chemistry of the Actinides, Vol.4 (Freeman, A.J. and Keller, C. eds.) Elsevier Science Publishers B.V., Amsterdam, 1986, p413.
(2) Kraus, K.A. and Nelson, F., AECD-1864, U.S. At. Energy Commission (1948).
(3) Kraus, K.A., Proc. Int. Conf. Peaceful Uses At. Energy, Vol.7, Geneva, 1955, p245 (1956).
(4) Moskvin, A.I., Sov. Radiochem., 13, 700 (1971).
(5) Sevost'yanova, E.P. and Khalturin, G.V., Sov. Radiochem., 18, 738 (1976).
(6) Maya, L., Inorg. Chem., 22, 2093 (1983).
(7) Bidoglio, G., Tanet, G. and Chatt, A., Radiochim. Acta, 38, 21 (1985).
(8) Lierse, Ch., Treiber, W. and Kim, J.I., Radiochim. Acta, 38, 27 (1985).
(9) Rösch, F., Milanov, M., Hung, T.K., Ludwig, R., Buklanov, G.W. and Khalkin, V.A., Radiochim. Acta, 42, 43 (1987).
(10) Nakayama, S., Arimoto, H., Yamada, Y., Moriyama, H. and Higashi, K., Radiochim. Acta, 44/45, 179 (1988).
(11) Nagasaki, S., Tanaka, S. and Takahashi, Y., J. Radioanal. Nucl. Chem., 124, 383 (1988).
(12) Neck, V., Kim, J.I. and Kanellakopulos, B., to be published in Radiochim. Acta.
(13) Strickert, R., Rai, D. and Fulton, R.W., ACS Symp. Ser., 246, p135 (1984).
(14) Rai, D., Swanson, J.L. and Ryan, J.L., Radiochim. Acta, 42, 35 (1987).
(15) Nakayama, S. and Banba, T., J. Nucl. Sci. Technol., 26, 607 (1989).
(16) Scatchard, G., Chem. Rev., 19, 309 (1936).
(17) Grenthe, I. and Wanner, H., Report NEA-TDB-2.1, OECD Nuclear Energy Agency, 1989.
(18) Wanner, H., Radiochim. Acta, 44/45, 325 (1988).

Table 1 Literature data on solubility product and hydrolysis constants of neptunium(V)

Method	Medium	I[(a)]	T(°C)[(b)]	$\log K_{sp}$	$\log\beta_1$	$\log\beta_2$	Ref.
solubility		0.1	25	-8.85	4.93		(2)
titration	NaCl	0.1	RT	-9.2			(3)
solubility		0.2	20	-9.0	3.92		(4)
potentiometry	$NaNO_3$	0.02		-9.73	5.1		(5)
solubility	$NaClO_4/NaHCO_3$	1.0	25		4.68		(6)
extraction	$NaClO_4/NaHCO_3$	0.2	25		4.16		(7)
solubility	$NaClO_4$	1.0	25	-8.81	2.33	4.89	(8)
electromigration	$NaClO_4$	0.1	25		3.55	6.05	(9)
solubility	$NaNO_3$	0.01	RT	-10.7	5.7	8.6	(10)
electrophoresis		0.1	RT		6.0	9.9	(11)
		0.005			5.7	9.2	
solubility	$NaClO_4$	3.0	25	-9.85(cr)	3.18	5.15	(12)
		1.0		-9.30(am)	2.67	4.41	
		0.1		-8.56(am)	2.44	4.10	

(a) I: ionic strength, (b) T: temperature, RT: room temperature

Table 2 Solubility product (K_{sp}), and first and second hydrolysis constants (β_1,β_2) of neptunium(V) at room temperature

ionic strength	$\log K_{sp}$	$\log\beta_1$	$\log\beta_2$
0.012	-8.1±0.1	3±1	(a)
0.10	-9.25±0.02	3.3±0.4	6.1±0.7
0.40	-9.78±0.08	3.4±0.2	5.5±0.3
0.80	-10.9±0.06	4.3±0.6	(a)

(a) Large errors were associated.

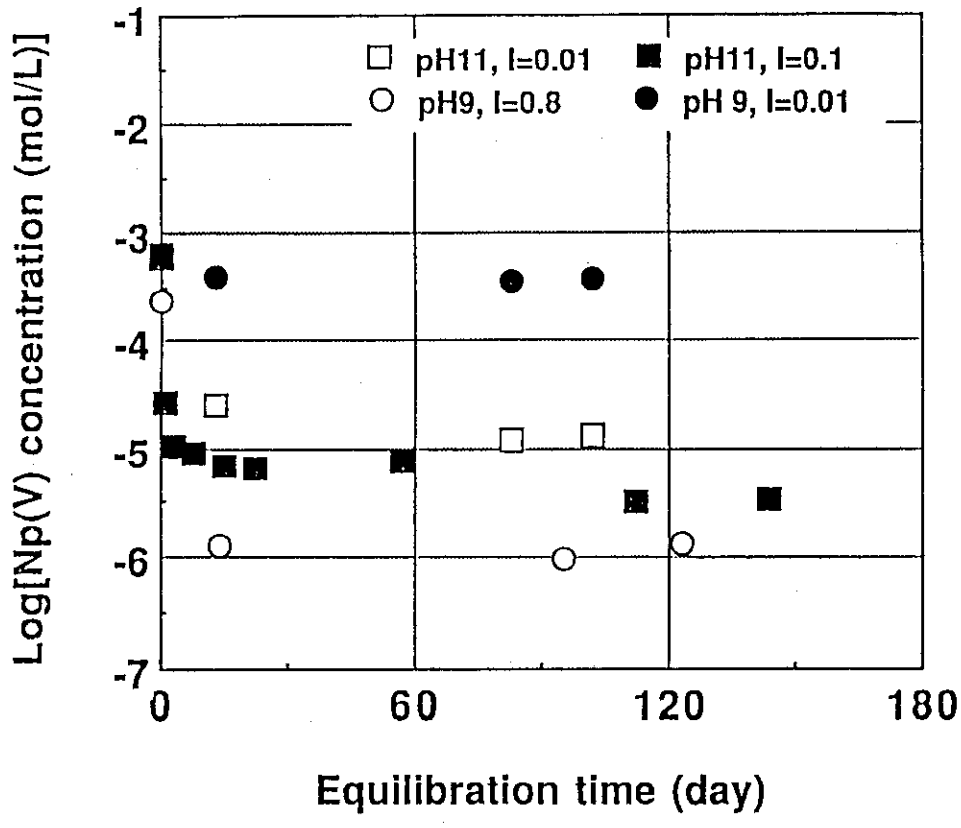

Fig. 1 Neptunium(V) concentrations in $NaClO_4$ solutions as a function of equilibration time.

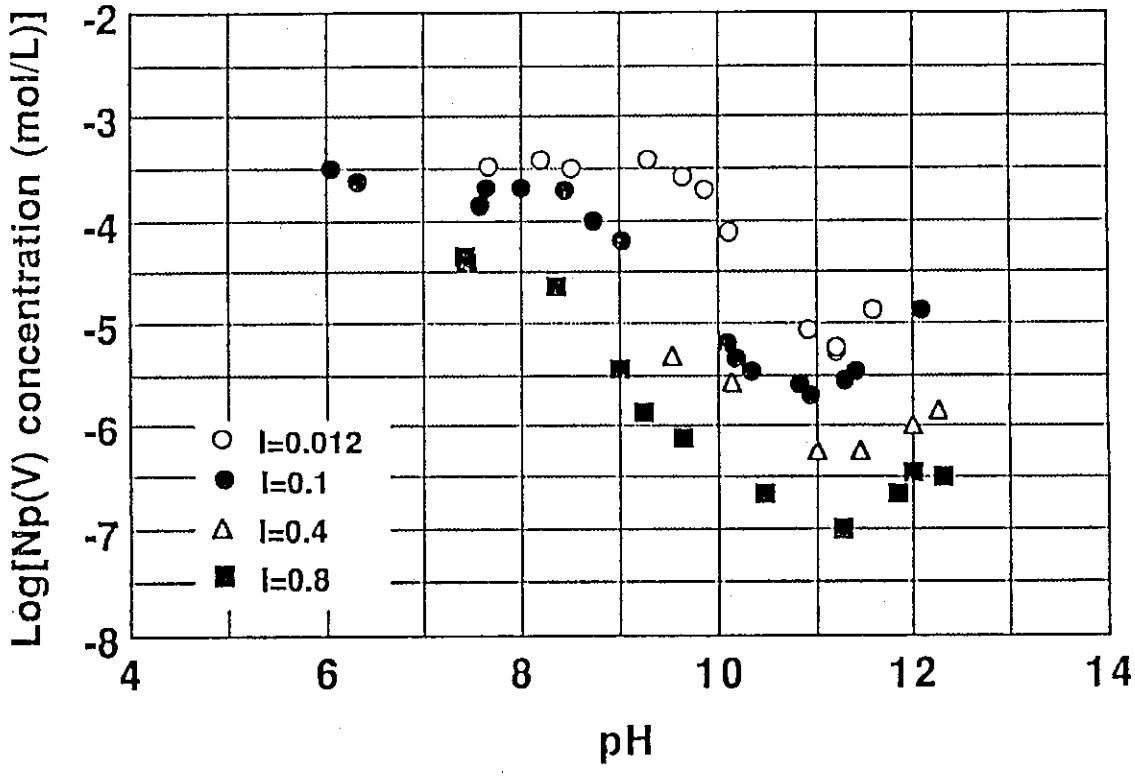

Fig. 2 Solubility of neptunium(V) hydroxide in $NaClO_4$ solutions.

2.2 Nuclide Migration and Retardation

2.2.1 Column Tests for Actinides in the URL, Canada

M. Kumata

INTRODUCTION

Geochemical processes such as diffusion, oxidation-reduction kinetics, colloid formation and precipitation play an important role in the transport of radionuclides from radioactive waste disposal facilities. To predict the transport of specific nuclides under deep geological conditions, experimental efforts should be made under in-situ conditions.

A new experimental system that would be able to perform column tests under in-situ conditions was developed under a JAERI/AECL cooperative program. The experimental system was installed in an experimental room excavated specially for the program at a 240 m level of the Underground Research Laboratory (URL) constructed in Precambrian batholith near Pinawa, Manitoba, Canada.

The system was designed to maintain the original geochemical conditions of rock and groundwater that will be used in the experiments. A controlled atmosphere glove box was set in the room. Nitrogen gas was used to maintain an inert atmosphere within the glove box. The oxygen content of the glove box was reduced to a few ppm by volume.

The column test for technetium, one of important elements for the safety assessment on the geological disposal of high-level radioactive waste, has been performed by using this experimental system. The result showing strong sorption of Tc on column materials suggests that the system maintained successfully the original geochemical conditions of rock and groundwater[1].

Column tests for actinides were performed in this experimental system by using crushed granitic rock and groundwater obtained from a fracture zone at a depth about 250 m.

EXPERIMENTAL

The most highly fractured sections of pink colored granitic rock core recovered from the Fracture Zone were selected for the column tests.

The selected sections of core were wet-crushed and wet-sieved using deoxygenated groundwater from the fracture zone. The 180-850 μm fraction was selected for the column tests. Chemical composition of this sample was shown in Table 1. During these procedures, the rock samples were handled carefully to minimize contact with air.

Table 1 Chemical composition of the rock sample filled in the columns*

Component	Weight %
Na_2O	3.02
K_2O	6.33
MgO	0.62
CaO	0.90
Al_2O_3	13.6
SiO_2	74.8
TiO_2	0.183
P_2O_5	0.060
MnO	0.016
Fe_2O_3	1.65
LOD**	< 0.10
LOI***	0.63

* Crushed rock sample (180-850 μm fraction)

** LOD: Loss on drying at 110°C

*** LOI: Loss on ignition at 1000°C

The groundwater was directly introduced into the system from the fracture zone through the Borehole to supply the water without contact with air. During the experimental period, Eh, pH, conductivity, temperature and pressure of the groundwater were monitored by an on-line system in the experimental room (Photo. 1).

The columns used in these experiments were made of stainless steel sized 2.54 cm in diameter and 20 cm in length. The column surface was carted with Teflon. Separate aliquots of groundwater, taken from fracture zone, were spiked with ^{237}Np, ^{238}Pu and ^{241}Am, in an anaerobic chamber, and injected into individual columns at a pressure of 0.7 MPa

by the supplied groundwater using a hydraulic accumulator. Tritiated heavy water was added to the aliquots to monitor the flow of the groundwater through the column. The flow rate was controlled by a timer device which co-ordinates the operation of the solenoid valves. About 110 ml of the solution was injected in to the column.

RESULTS AND DISCUSSION

In all cases, strong sorption of the actinides on column materials was observed. Only very small fractions of the injected radionuclides were eluted from each column in the tritium breakthrough regions. Following this initial breakthrough, no further elution of the radionuclide was observed over the 200 day duration of the experiments. Radionuclide distribution analysis on the column materials of each column showed that most of the nuclides were remained firmly near the inlet of the column (Fig. 1). These results suggested rapid chemical sorption interaction of the dissolved radionuclides in groundwater with the minerals and very slow desorption during the transport through fractures of granitic rock.

REFERENCE

(1) M. Kumata and T.T. Vandergraaf: Nuclides Migration Tests under deep geological conditions, in Proc. Int. Symp. Advanced Nuclear Energy Research, pp.414-419, 1991.

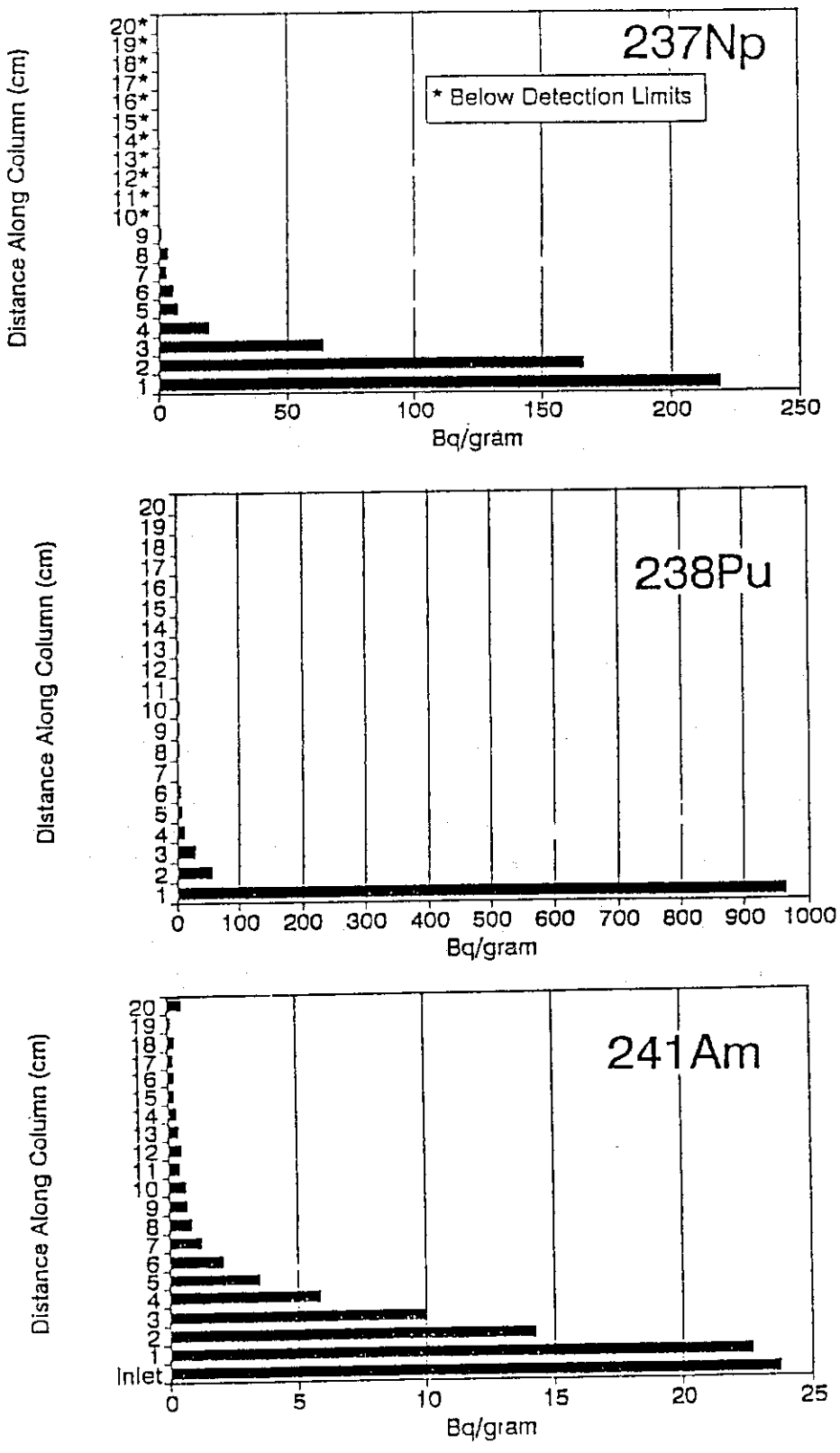

Fig. 1 Distribution of actinides in each column after more than 200 days of continuous elution.

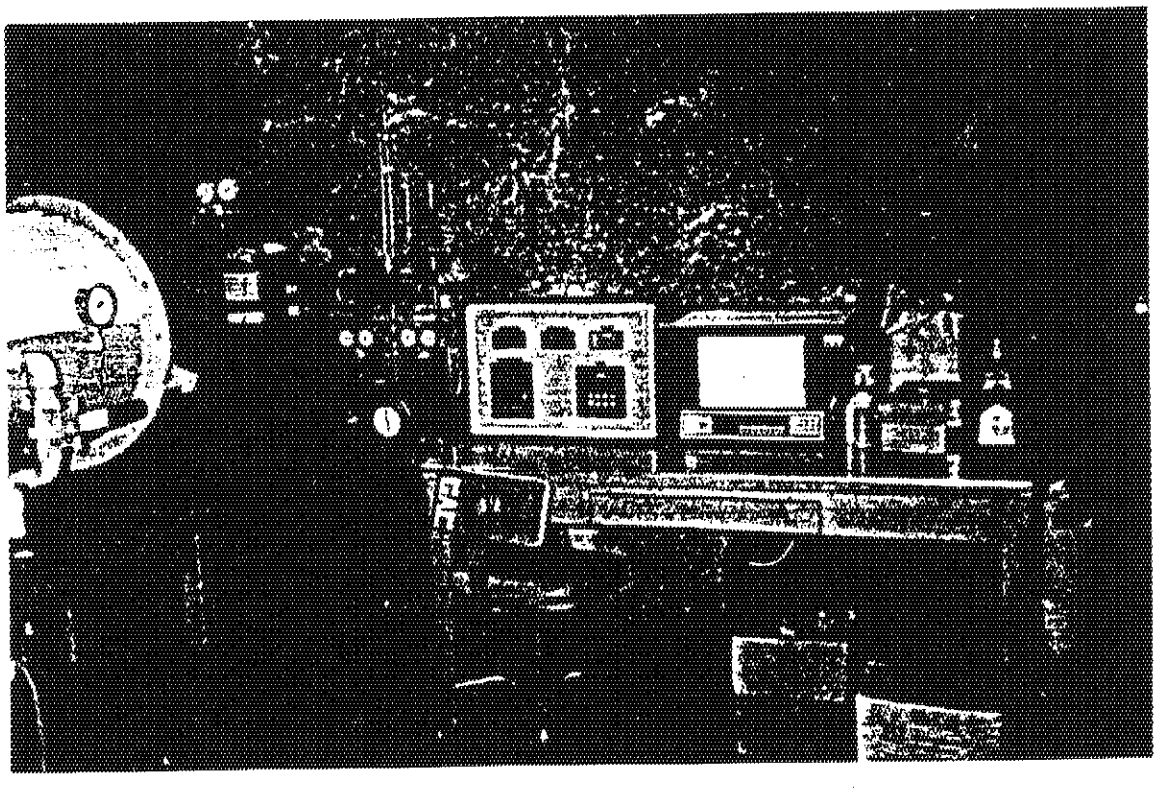

Photo. 1 Manifold containing the pH, Eh and conductivity probes used for the on-line monitoring of these parameters. The equipment in the foreground consists of the output devices and a recording device.

2.3 Long-term Radionuclide Fixation Mechanisms

2.3.1 Redistribution of Strontium during Goethite Crystallization from Amorphous Iron Hydroxides

Y. Sakamoto

INTRODUCTION

In the engineered barrier for high level radioactivewaste, a large amount of iron will be dissolved from a canister and overpack after long term emplacement. Radionuclides are adsorbed on amorphous or crystalline iron compounds arose by precipitation. If amorphous iron compounds are transformed into crystalline one after radionuclides is adsorbed on them, the radionuclides will be redistributed on the crystalline one. Consequently, it is important to study the redistribution behavior of radionuclides during transformation in iron compounds.

The strontium adsorption experiment was conducted under the crystallization from amorphous iron hydroxides to goethite. After adsorption, a sequential extraction was applied to study a degree of association between strontium and iron compounds. Using the dried goethite powder with three kinds of crystallinity, a simple adsorption experiment without goethite crystallization was also performed to compare the adsorption behavior of strontium.

EXPERIMENTAL

Solution of iron nitrate with the concentration 0.2 M was prepared in a 500 ml breaker. The solution pH was adjusted to 12 with 5 M and 1 M sodium hydroxide solutions to make amorphous iron hydroxide precipitates. Each 50 ml of the suspensions was transferred to polyethylene centrifugation tubes. The iron precipitates were centrifuge-washed three times with deionized water.

Strontium nitrate solution with 3×10^{-3} mol/L was made in 0.03 M sodium perchlorate solution. The solution pH was adjusted to 12 as same condition of above iron precipitation. The strontium solutions of 50 ml were subdivided into each above centrifugation tubes including the wet iron precipitates. They were kept at 40°C in a thermostated oven for 12, 24, 36, 48, 96, 120 and 168 hours, respectively. After the aging them,

the phases were separated by centrifugation at 3000G for 10 min. The supernatant was filtrated with 0.45 μm Millipore Millex filter. The strontium concentration in the solution was measured with ICP. Adsorption ratio of strontium onto iron precipitates was calculated with difference in the strontium concentrations before and after adsorption experiment. The precipitates were washed with deionized water and dried with a freeze dryer. The dried solid products were crashed with an agate mortar. The content of goethite in a unit weight of iron precipitate was measured by peak area at 890 cm^{-1} in an infrared diffuse reflectance spectrum. The crystallinity in percentage for each sample was determined from relative value for saturated peak area that was defined as 100% crystallinity of goethite.

The iron precipitates were sequentially extracted with following three steps;

(1) Ion exchangeable: (Fi)
The precipitates of 0.05g were extracted at room temperatures for 1 hour with 20 ml of magnesium chloride solution (1M $MgCl_2$, pH 7).

(2) Bound to amorphous iron hydroxides: (Fa)
The precipitate from fraction (1) was extracted with 20 ml of 0.04M $NH_2OH \cdot HCl$ in 25% HOAC solution at 90°C for 5 hours.

(3) Residual: (Fr)
The residue on the filter from fraction (2) was digested with a HF-$HClO_4$ mixture solution.

In this paper, the fractions are named as Fi, Fa and Fr, respectively.

To study the difference of strontium adsorption behavior by existence of goethite crystallization, a simple adsorption experiment was conducted with dried iron precipitates. The solid samples were freshly prepared without strontium solution. The crystallinities of them were 0, 55 and 100%, respectively. After adsorption, the iron compounds were sequentially extracted with the same manner as described above.

RESULTS AND DISCUSSION

The correlation between aging time and the goethite crystallinity was shown in Fig. 1. The goethite crystallinity was achieved 100% for 90 hours. The strontium adsorption ratios against aging time of the iron precipitates are also illustrated in Fig. 1. The strontium adsorption ratio was almost 98% up to 50 hours of aging time. After crystallization

became close to 100%, however, the ratio was decreased to about 60%. The result implies that the strontium adsorbed on the amorphous iron hydroxides are released with the goethite crystallization and are redistributed on the crystalline goethite.

Figure 2 shows the relative distribution for strontium in the sequential extraction from iron precipitates with various crystallinities. In the adsorption experiment with the goethite crystallization (see Fig. 2(a)), the ion exchange fraction was from 60% to 80%. The Fa fraction decreased with goethite crystallization. For the samples of simple adsorption, almost strontium was extracted in the Fi and Fa fraction as shown in Fig. 2(b). These results imply that the ion exchange and association to amorphous hydroxides are predominant for the strontium adsorption. It is agreement with the strontium adsorption behavior reported by Jackson and Inch[1]. In the case of adsorption accompanied with goethite crystallization, a significant amount of residual fraction was recognized to increase with crystallization, as shown in Fig. 2(a). On the other hand, this fraction did not exist in the simple adsorption. Comparing Fig. 2(a) with Fig. 2(b), it is likely that some amount of strontium adsorbed on amorphous hydroxides remained in crystalline goethite during crystallization. Vanek and Jaedináková reported that many discontinuities resulting from defects of various kinds on goethite surface and the occurrence of relatively strong bonding forces on goethite[2]. The strontium may be trapped into these kinds of discontinuities when amorphous hydroxides are transformed to crystalline goethite.

From above results, radionuclide released from waste glass have possibility to be incorporated into iron compounds when amorphous iron compounds are transformed into crystalline one. This phenomenon becomes one kind of fixation of radionuclides.

REFERENCES

(1) R.E. Jackson and K.J. Inch, Radionuclide Adsorption in Hydrogeochemical Process Affecting the Migration of Radionuclides in a Fluvial Aquifer at the Chalk River Nuclear Laboratories, Sci. Series No.4, Inland Waters Directrorate, Environmental Canada, Ottawa, 41 (1980).

(2) K. Vanek and V. Jaedináková, A study of the strontium ions on α-FeOOH, Collection Czechoslovak Chem. Commun., Vol.51, 2455 (1986).

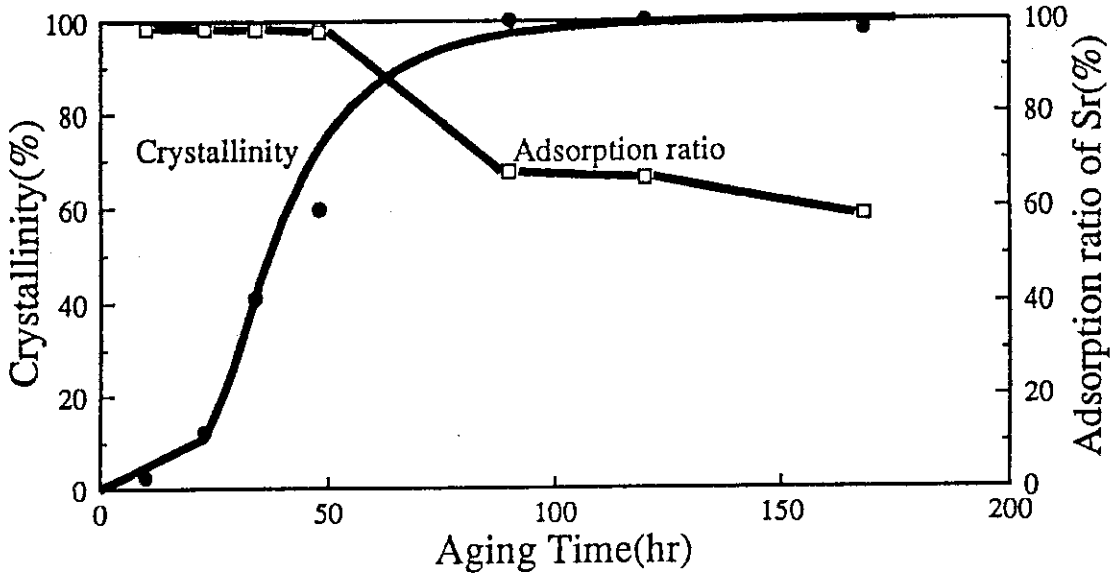

Fig. 1 Time evolution of crystalline goethite and adsorption ratio of strontium on iron precipitates

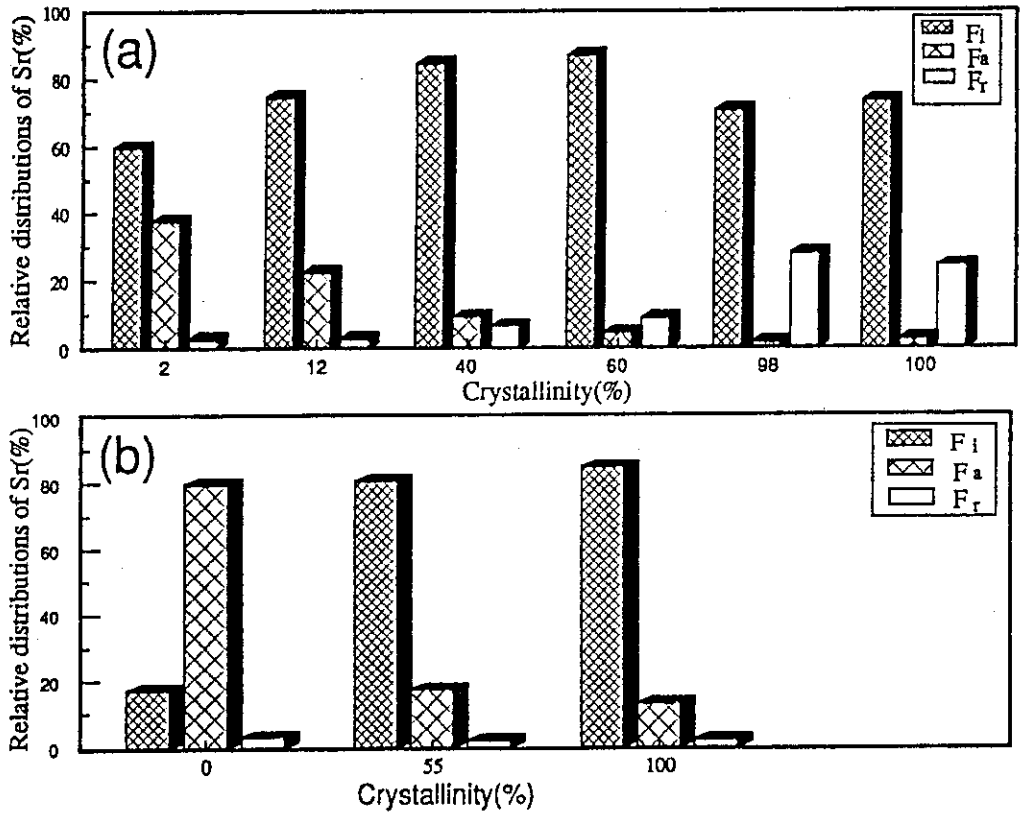

Fig. 2 Relative distributions of strontium in sequential extractions
(a) The adsorption accompanied with goethite crystallization
(b) The simple adsorption without goethite crystallization
Fi: ion exchange fraction which was extracted by 1M $MgCl_2$ solution
Fa: The fraction which was extracted by 0.04M $NH_2OH \cdot HCl$ in 25% HOAC solution
Fr: The residual fraction which was digested by $HF-HClO_4$ solution

2.3.2 Determination of Crystallinity of Goethite by X-ray Diffractometry and Infrared Spectroscopy

T. Nagano

INTRODUCTION

Deep groundwaters around repositories of high-level radioactive wastes are considered to contain a large quantity of iron dissolved from engineered barrier materials such as canister or overpack. The dissolved iron species are precipitated as amorphous iron compounds because of the low solubility in near-neutral aqueous solutions. The initial amorphous precipitates will be gradually transformed to crystalline phases for a long period, so there are also many iron oxides or hydroxides with various crystallinity around the repositories. Some radionuclides leached from waste glasses are expected to be fixed with the iron compounds by coprecipitation or sorption, and have certain chemical stability in the geological disposal environment. Then it is very important to study the interactions between the iron compounds and radionuclides. Nakayama and Sakamoto studied sorption of neptunium on naturally-occurring iron-containing minerals, namely hematite, goethite, magnetite and biotite[1]. They found that goethite shows a stronger sorption behavior in near-neutral solutions than the others. But the samples they used were crystalline phases. Since the amorphous iron compounds are considered to have a larger sorption capacity than the crystalline ones due to their active surfaces, it is also quite important to study the interactions between the amorphous iron compounds and the radionuclides. In this study, at the first step to evaluate a sorption behavior on the non-crystalline goethite with various crystallinity, a close determination of the goethite crystallinity was performed by synthesizing goethite from ferric nitrate solution in a laboratory.

EXPERIMENTAL

Amorphous iron hydroxides were precipitated from 0.1M ferric nitrate solutions by adding 2M sodium hydroxide solutions till pH 13. The solutions were stirred continuously during the pH adjustment to avoid local precipitation. The suspensions were subdivided into 50ml polyethylene

bottles and in total 20 bottles were prepared. They were then kept in an electric thermostated oven at 40°C to incubate the suspensions. At a certain interval, one of the bottles was taken out, and the precipitate was centrifuge-washed two times with deionized water, and freeze-dried. After drying, the samples were slightly crushed by agate mortar to attain uniform grain size.

Crystalline phases of the resulting precipitates were characterized by X-ray diffractometry (XRD) using Rigaku powder diffractometer (CuKα radiation, 50kV, 35mA), which was equipped with SUN data processing system. Infrared diffuse reflectance spectra (250-4000 cm^{-1}) of the samples were measured by JEOL FT-IR instrument (JIR-3505). Diffuse reflectance spectroscopy (DRS) is a useful method for quantitative analyses because of their easier sample preparation than KBr pellet methods. A half spherical mirror (Spectra Tech's Collector) was installed in the spectrometer to collect diffuse reflectance light from the sample surface. KBr powders were used as reference. Stainless small pan containing about 500mg of powdered samples was set up into the diffuse reflectance equipment. After purging the sample container by dried air, 100 measurement scans were conducted with a spectral resolution of 4 cm^{-1}.

RESULTS AND DISCUSSION

XRD patterns for samples with different incubation time are shown in Fig. 1. Only goethite was identified as a crystalline phase in this figure. It can be said that all these peaks associated with goethite increase their intensities as the incubation time increases. This result indicates an evidence for the crystallization of goethite with the incubation time. Two broad bands observed around 34 deg (2.63Å) and 61.5 deg (1.51Å) in SG0 are considered to be due to amorphous iron hydroxides, generally called ferrihydrite[2,3]. This phase is considered to be a source of goethite crystal because appearances and increases of goethite peaks are observed around the two bands.

Infrared diffuse reflectance spectra for the precipitates with different incubation time are shown in Fig. 2. A sharp peak at 1384 cm^{-1} observed in all spectra is due to incorporated or adsorbed NO_3^-. A peak at 1265 cm^{-1} in SG3, SG10 and SG24 is due to adsorbed HCO_3^-. A weak band at 850 cm^{-1} in SG0 spectrum is due to $NaNO_3$. It is clearly

observed that the following 4 peaks associated with goethite increase their absorptions with the incubation time, that is 3155 cm^{-1} due to O-H stretching vibration, 890 and 795 cm^{-1} due to O-H bending vibration and 640 cm^{-1} due to Fe-O lattice vibration. On the other hand, decreases of absorptions of the following 4 peaks with the incubation time are apparent, i.e., 3400 cm^{-1} due to stretching vibration of incorporated H_2O into the goethite precipitates, 1630 cm^{-1} due to bending vibration of incorporated H_2O[4] and 1510 and 1345 cm^{-1} due to coordinated or adsorbed carbonate.

From these results, it can be said that during the incubation the initial precipitates gradually exclude the incorporated molecular water outside the amorphous iron hydroxides, which exhibits the infrared absorptions at 3400 and 1630 cm^{-1}. Simultaneously goethite crystal is gradually formed, which is observed as increases of infrared absorption at 3155, 890, 795 and 640 cm^{-1}. Therefore, these are clear evidences that the crystallization of goethite is a dehydration reaction of amorphous iron hydroxides.

Crystallinity of goethite were determined by XRD and infrared spectroscopy. An XRD peak height at 21 deg (4.18Å), which has the strongest intensity among the goethite reflection, and an infrared peak area at 890 cm^{-1} were chosen as indicators of goethite crystallinity. The XRD peak heights were calculated after smoothing the diffraction patterns and removing the background, and the infrared peak areas after transforming the transmittance to absorbance by Kubelka-Munk function and removing the background. The results are shown in Fig. 3. In both analyses, the crystallinity increases with the incubation time till about 1 day and saturate beyond 1 day, so the saturated XRD peak height and infrared peak areas are tentatively defined as 100% of crystallinity. It is also observed that the crystallinity determined by XRD are slightly higher than those by infrared spectroscopy and that as a result a rate of increase of goethite crystallinity by XRD is also slightly larger than that by infrared spectroscopy.

A calibration curve of the goethite crystallinity is necessary for the determination of accurate crystallinity. Since non-crystalline material is composed of both crystalline parts and amorphous parts, their crystallinity (x: content of crystalline parts (wt%)) are usually defined as,

$$x = mc/(mc+ma) = mc/m$$

where mc, ma and m represent weight of crystalline parts, weight of amorphous parts and total weight of the material, respectively. In this study, the initial precipitates are regarded as the amorphous parts, named as SGa, and the last one with 6 weeks of incubation time as the crystalline parts, named as SGc. Mixtures of SGc and SGa with different contents of SGc, i.e., 0, 20, 40, 60, 80 and 100 wt%, were prepared and subjected to XRD and infrared diffuse reflectance spectroscopy. Then the calibration curves of goethite crystallinity were drawn using data of the two analyses, i.e., peak heights at 21 deg of XRD and peak areas at 890 cm^{-1} of infrared spectra (See Fig. 4). It is clear that infrared peak areas at 890 cm^{-1} increase proportionally to the SGc content. On the other hand, in the case of XRD analysis the linearity does not hold well. Therefore, using the data of XRD, correction is necessary for the accurate goethite crystallinity. This is a reason for the slightly higher crystallinity by XRD analyses than by infrared spectroscopy (See Fig. 3). Consequently, the infrared peak area around 890 cm^{-1} is defined as the crystallinity of goethite in this study.

REFERENCES

(1) Nakayama, S. and Sakamoto, Y.(1991) Sorption of neptunium on naturally-occurring iron-containing minerals: Radiochimica Acta, 52/53, 153-157.

(2) Towe, K.M. and Bradley, W.F. (1967) Mineralogical constitution of colloidal "hydrous ferric oxides.": J. Colloid Interface Sci., 24, 384-392.

(3) Eggleton, R.A. and Fitzpatrick, R.W. (1988) New data and a revised structural model for ferrihydrite: Clays and Clay Minerals, 36, 111-124.

(4) Glemser, O. (1959) Structure of some hydroxides and hydrous oxides: Nature, 183, 943-944.

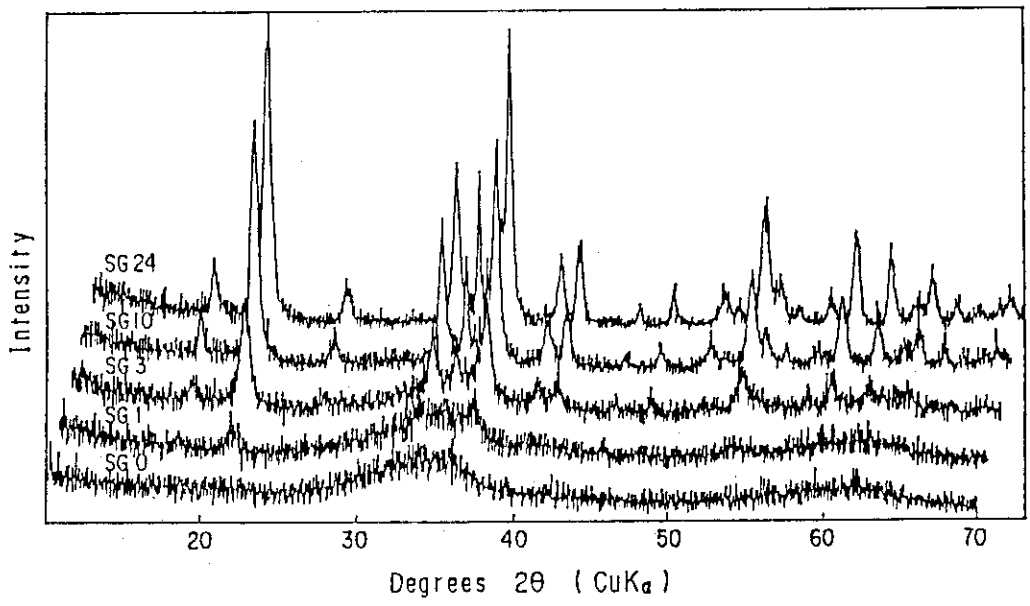

Fig. 1 X-ray diffraction patterns for the synthesized goethite with 0, 1, 3, 10 and 24 hours of incubation time, labelled as SG0, SG1, SG3, SG10 and SG24, respectively. Only goethite was identified as a crystalline phase. Two broad bands around 34 and 61.5 deg in SG0 are due to amorphous iron hydroxides.

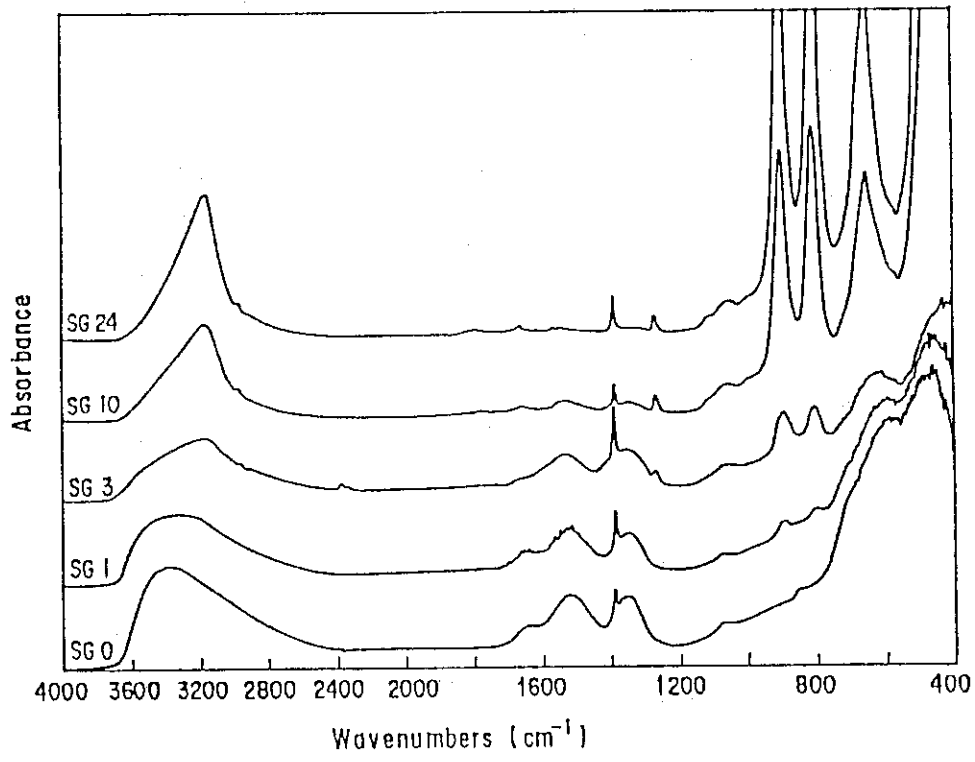

Fig. 2 Infrared diffuse reflectance spectra for the synthesized goethite with 0, 1, 3, 10 and 24 hours of incubation time, labelled as SG0, SG1, SG3, SG10 and SG24, respectively. Increases of absorptions of 4 peaks associated with goethite are obvious around 3155, 890, 795 and 640 cm^{-1}. A broad peak at 3400 cm^{-1} due to incorporated H_2O in amorphous iron hydroxides decreases its absorption with the time.

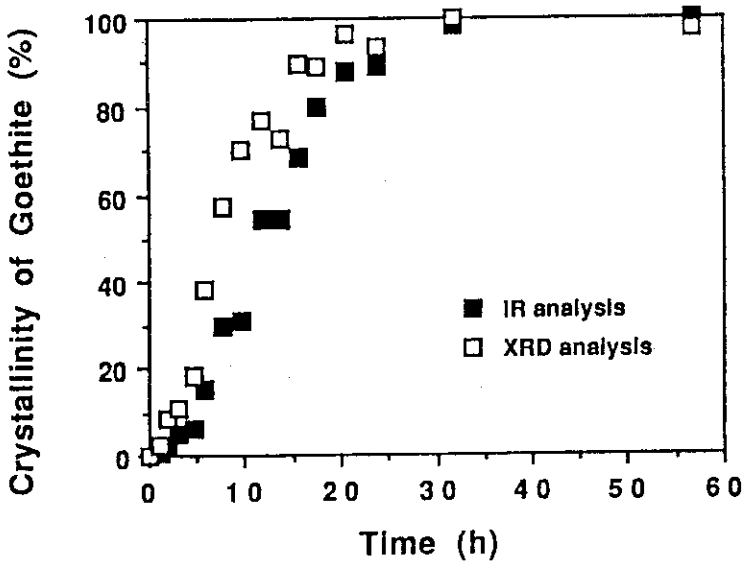

Fig. 3 Time evolution of goethite crystallinity determined by peak heights at 21 deg in XRD and peak areas at 890 cm^{-1} in infrared spectra. In both analyses, crystallinity increase with the incubation time till about 24 hours and saturate beyond that time. Crystallinity by XRD are slightly larger than those by infrared spectra.

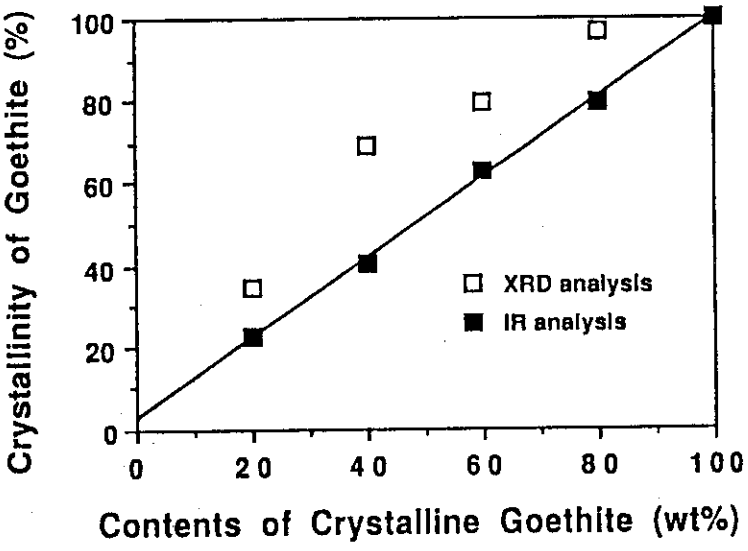

Fig. 4 Correlation between peak heights at 21 deg in XRD or peak areas at 890 cm^{-1} infrared spectra and contents of crystalline parts of goethite (wt%). Peak areas in infrared spectra can be treated as quantitative indicators, but correction is necessary in dermining the crystallinity by XRD.

3. Natural Analogue Study

3.1 Study on Role of ^{234}Th in Uranium Series Nuclides Migration

T. Ohnuki, S. Watanabe and T. Murakami

INTRODUCTION

It is known that there are differences in the pattern of uranium series disequilibria between locations, such as, the Koongarra ore deposit, Australia[1], the 'K' deposit, South Africa[2] and Yelirrie, Australia[3]. The $^{234}U/^{238}U$ activity ratios are always greater than one in the 'K' deposit and Yelirrie, where the activity disequilibria of ^{238}U and ^{234}U may result from preferential leaching of daugher nuclides of ^{238}U and α-recoil effects[4,5]. On the other hand, at Koongarra, a positive relationship of the $^{234}U/^{238}U$ to $^{230}Th/^{238}U$ activity ratios indicates that ^{238}U migrates faster than ^{234}U, and this is inconsistent with expected activity disequilibria which result from the preferential leaching.

In the present study, we assume that some portion of the ^{234}Th is irreversibly fixed to the rock, and ^{234}U resulting from the decay of the fixed ^{234}Th is also firmly bound. We estimate the role of ^{234}Th by using a mathematical model of the migration of uranium series nuclides.

MIGRATION MODEL

Figure 1 schematically shows the migration behavior of the uranium series nuclides that is proposed in the present study. We assume that there are three sites in the Koongarra medium where the uranium series nuclides are found. The first is a liquid site where the uranium series nuclides migrate with water flow and dispersion (the first line in Fig. 1). The second is a solid side S where the nuclides are accommodated reversibly by, for example, surface adsorption (the second line in Fig. 1); the nuclides may be desorbed easily. The third is a solid site F where the uranium series nuclides are accommodated irreversibly by, for example, fixation in crystallographic sites (the third line in Fig. 1); the uranium series nuclides cannot be desorbed. The flow of the nuclides to be noted in Fig. 1 is as follows: the parent nuclide, ^{238}U in rock, dissolves into water, or decays to ^{234}Th. A fraction of the ^{234}Th may

dissolve into water because of the α-recoil effects. However, because ^{234}Th is highly adsorptive, ^{234}Th in the groundwater is readsorbed onto the rock. Some of the ^{234}Th in the rock, both readsorbed and directly decayed, is fixed at the site F. Thus ^{234}U resulting from the decay of the irreversibly fixed ^{234}Th is much less able to be desorbed than ^{238}U.

The deriving equations of the uranium series nuclides are expressed by the following equations:

$$\frac{\partial}{\partial t}U_{238,W} = -\frac{v}{R_1}\frac{\partial}{\partial x}U_{238,W} - \lambda_1 U_{238,W}$$

$$\frac{\partial}{\partial t}U_{234,W} = -\frac{v}{R_3}\frac{\partial}{\partial x}U_{234,W} - \lambda_3 U_{234,W} + \lambda_2\lambda_1(f_W+f_M)U_{238,W}$$

$$\frac{\partial}{\partial t}U_{234,F} = \lambda_2 f_F \lambda_1 U_{238,W} - \lambda_3 U_{234,F}$$

$$\frac{\partial}{\partial t}Th_{230,F} = \lambda_3 \cdot R_3 \cdot U_{234,F}$$

where

$$f_M = \frac{R_1-1}{R_1}\frac{1}{\lambda_2}$$

$$f_W = \frac{1}{\lambda_2+k_{SF}^{\cdot}}\frac{2R_1-1}{R}$$

$$f_F = \frac{k_{SF}^{\cdot}}{\lambda_2(\lambda_2+k_{SF}^{\cdot})}\frac{2R_1-1}{R_1}$$

$$k_{SF}^{\cdot} = \frac{R_2-1}{R_2}k_{SF,2}$$

v : water velocity ($m \cdot yr^{-1}$),
θ : water content (-),
ρ : bulk density ($g \cdot cm^{-3}$),
x : distance (m),
t : time (yr),
R_i : retardation factor of ith nuclide, equal to $1+(\rho/\theta)K_{di}$,
K_{di}: distribution coefficient of ith nuclide ($ml \cdot g^{-1}$).

CALCULATIONS

Time dependent concentration profiles of the uranium series nuclides

were calculated for increase in the migration distance. The relationships between the $^{234}U/^{238}U$ and the $^{230}Th/^{238}U$ activity ratios (ARs) were then examined to see the effect of changing the ^{234}Th fixation rate constants on the migraton velocities of ^{238}U and ^{234}U[1].

It was assumed in the calculations that the nuclides were discharged at time 0 from their original position and the activities of the nuclides remained in equilibrium when they came into contact with water. The nunuclides were assumed not to be fixed at the original position.

We have also assumed that the distribution coefficients of ^{238}U and ^{234}U were the same (Table 1), and then varied the rate constants of ^{234}Th from the S to F sites. Thus we could simplify the calculations and demonstrate the effect of the presence of ^{234}Th on the nuclide migration at Koongarra. The other parameters used in the calculations are shown in Table 1.

RESULTS AND DISCUSSION

Figures 2a and 2b show the concentration profiles of the uranium series nuclides and the relationship between the $^{234}U/^{238}U$ and $^{230}Th/^{238}U$ ARs, respectively, when the rate constant of ^{234}Th from S to F sites is 12.0 (yr^{-1}). The concentration profiles show that the migration velocities of ^{238}U, ^{234}U and ^{230}Th are in the order of ^{238}U, ^{234}U, and ^{230}Th. The relationship between the $^{234}U/^{238}U$ and $^{230}Th/^{238}U$ ARs indicates a positive linear correlation. In Fig. 2b the upstream $^{234}U/^{238}U$ ARs are larger than those in the downstream, in agreement with values observed in the Koongarra ore deposit (Figs. 3a and 3b). Thus, the fixation of ^{234}Th to a rock can cause the apparent migration velocity of ^{234}U to be reduced relative to that of ^{238}U.

In quartz-chlorite schist, the host rock at Koongarra, quartz remains unchanged during weathering but chlorite is altered to vermiculite and then kaolinite and smectite[7] with iron minerals, ferrihydrite, goethite, and hematite being formed. In the "Koongarra dispersion fan"[8] the uranium concentrations have been shown to be directly related to the extent of the chlorite alteration[7]. Although we are not certain which minerals are responsible for the ^{234}Th fixation, they can be the clay and/or iron minerals previously discussed[1,7]. If the clay minerals are responsible, the possible S and F sites are the surfaces and the

interlayers of vermiculite and smectite, respectively. However, no data is available for the diffusion rates of Th from surfaces to the interlayers. Shirvington has suggested the possible incorporation of ^{234}Th into the octahedral sites of clay minerals[9].

If the iron minerals are responsible for the fixation, the possible S and F sites may be related to the reactions from the amorphous to crystalline iron minerals, i.e., ferrihydrite to goethite and hematite. Uranium in ferrihydrite is accessible to the groundwaters[10] and Th is less desorbed from ferrihydrite than U[11], therefore, the ferrihydrite surfaces are possible S sites. On the other hand, the half conversion of ferrihydrite to geothite and hematite takes 112 days at pH 7 and 24°C[12] corresponding to a rate constant of 2.3 yr^{-1} (see Fig. 4); groundwaters at Koongarra have pH values of 6.5 - 7.2[13] and the average monthly temperature is 25 - 29°C. Thus the crystallographic sites and/or impurities of goethite and hematite are possible F sites.

REFERENCES

(1) T. Ohnuki, T. Murakami, K. Sekine, N. Yanase, H. Isobe, Y. Kobayashi, in Scientific Basis for Nuclear Waste Manag. XIII, edited by V.M. Obersby and P.W. Brown, (Mater. Res. Soc. Proc. 176, Pittsburgh, PA, USA, 1990) p.607.

(2) R.S. Lively, "Uranium Series Disequilibrium in Three Surficial Uranium Deposits", M.S. Thesis, Michigan State Univ. USA, 1978.

(3) R.S. Lively, R.S. Harmon, A.A. Levinson and C.J. Bland: J. Geochem. Expl., 12, 57 (1979).

(4) R.L. Fleischer and O.G. Raabe: Geochim. Cosmochim. Acta 42, 973 (1978).

(5) Y. Eyal and R.L. Fleischer: Geochim. Cosmochim. Acta 49, 1155 (1965).

(6) G. Prowse: private communication.

(7) T. Murakami, H. Isobe and R. Edghill, this volume.

(8) A.A. Snelling, in Proceedings of IAEA International Symposium Uranium in the Pine Creek Geosyncline, edited by J. Ferguson and A.B. Goleby, (IAEA, Vienna, 1980) p.487.

(9) P.J. Shirvington: Geochim. Cosmochim. Acta 47, 403 (1983).

(10) P.L. Airey: Chem. Geol. 55, 255 (1986).

(11) T. Ueno: private communication.

(12) U. Schwertmann and E. Murad, Clays and Clay Minerals 31, 277 (1983).

(13) T. Payne, in Alligator Rivers Analogue Project 1st Annual Report, edited by P. Duerden, (Australian Nuclear Science and Technology Organization, Lucas Heights, NSW 2232, Australia, 1990) p.119.

Table 1 Parameters used in the calculation

Parameter	value
distance	200 m
time	1×106 yr
bulk density	1.6×103 kg m^{-3}
water content	0.1
water velocity	1.0 m·yr^{-1}

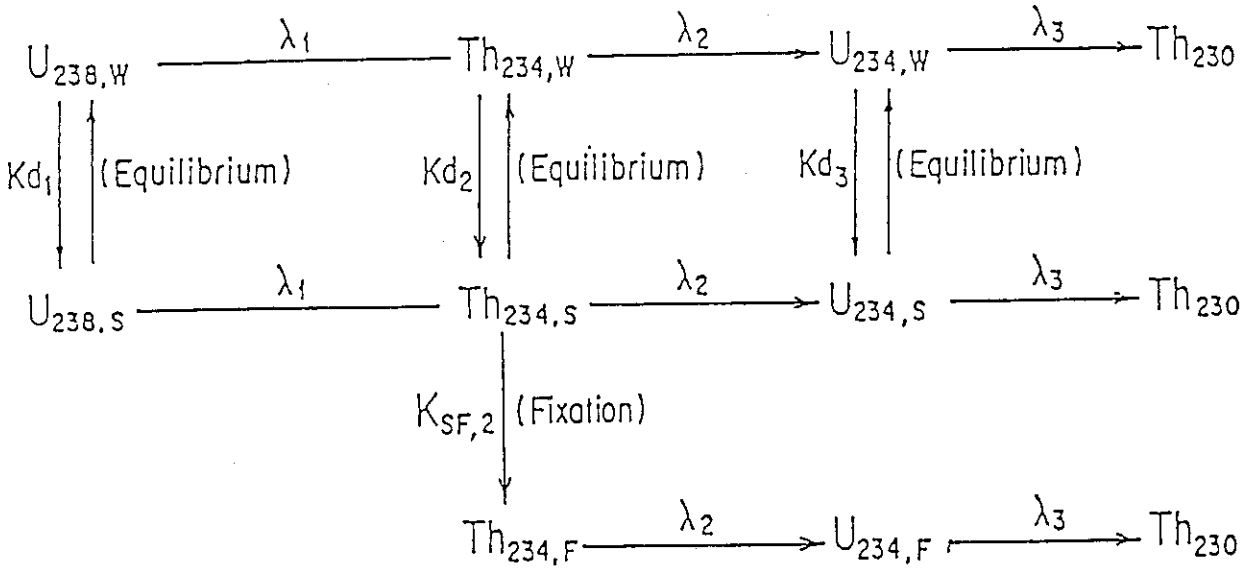

Fig. 1 Schematic flowsheet of uranium series nuclides migration for the modelling concept. U, Th are concentrations of U and Th (Bq L^{-1} or Bq g^{-1}). Subscripts W, S, F indicate the liquid site, loosely adsorption site, and tightly fixed site, respectively. $k_{Ws,i}$ and $k_{SW,i}$ are the adsorption and desorption rate constants of the ith nuclides (yr^{-1}); i=1; ^{238}U, i=2; ^{234}Th, i=3, ^{234}U, and $k_{SF,2}$ is the fixation rate constant of ^{234}Th (yr^{-1}). λ_i is the decay constant of the ith nuclide (yr^{-1}).

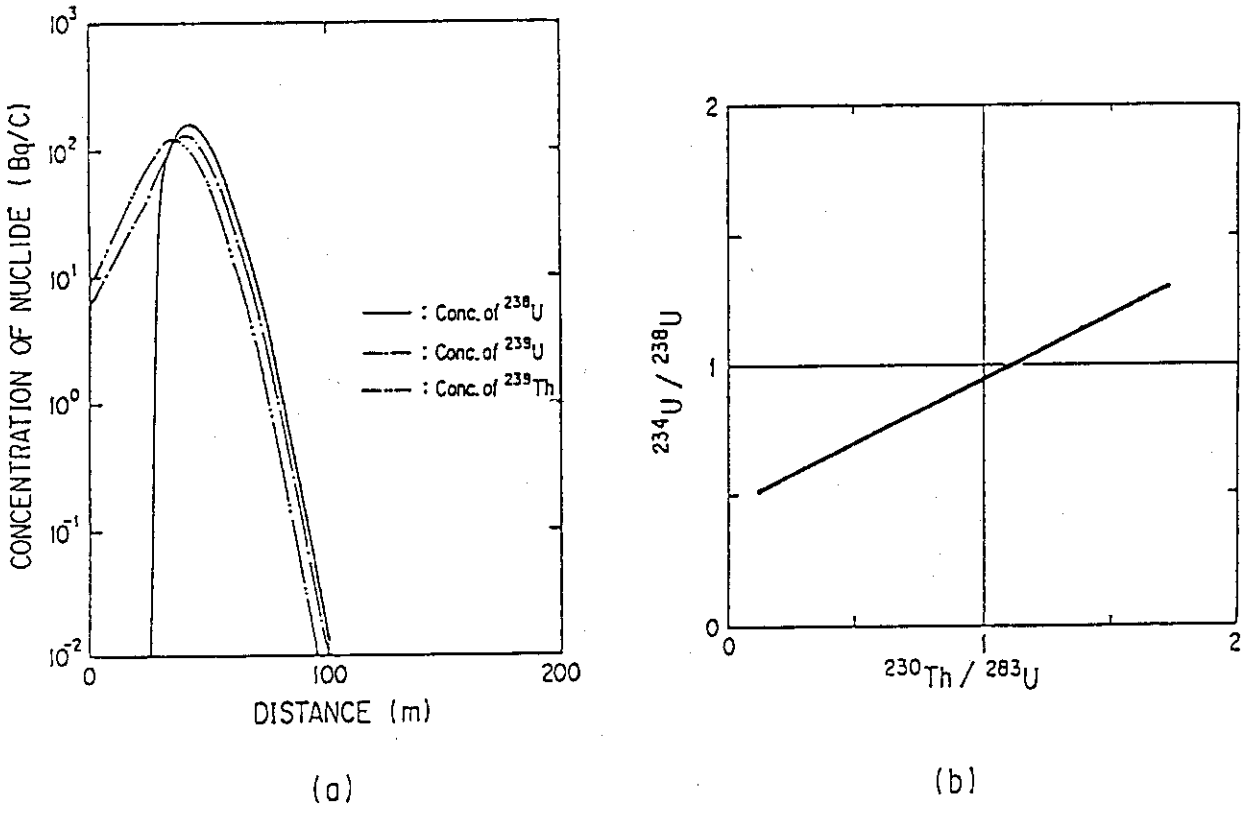

Fig. 2 Concentration profiles of uranium series nuclides (a) and the relationship between the $^{234}U/^{238}U$ and $^{230}Th/^{238}U$ activity ratios (b) at 1 million years with the ^{234}Th fixation rate being 12.0 yr^{-1}.

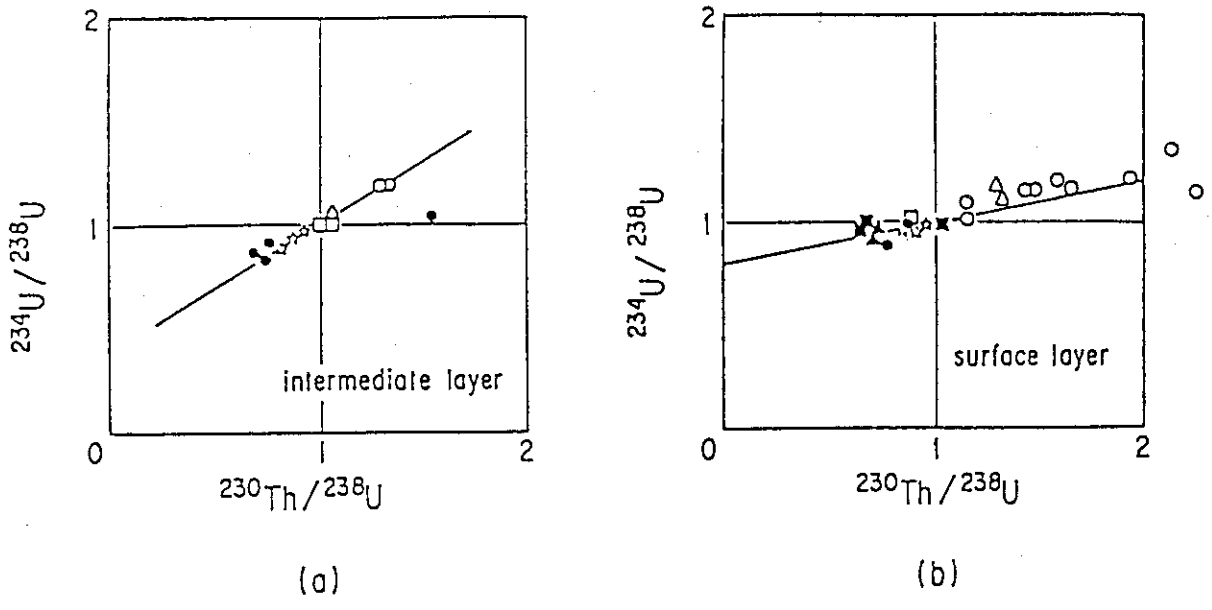

Fig. 3 The relationship between the $^{234}U/^{238}U$ and $^{230}Th/^{238}U$ activity ratios observed in the intermediate layer (a) and the surface layer (b) at Koongarra. (From Ohnuki et al.[1])

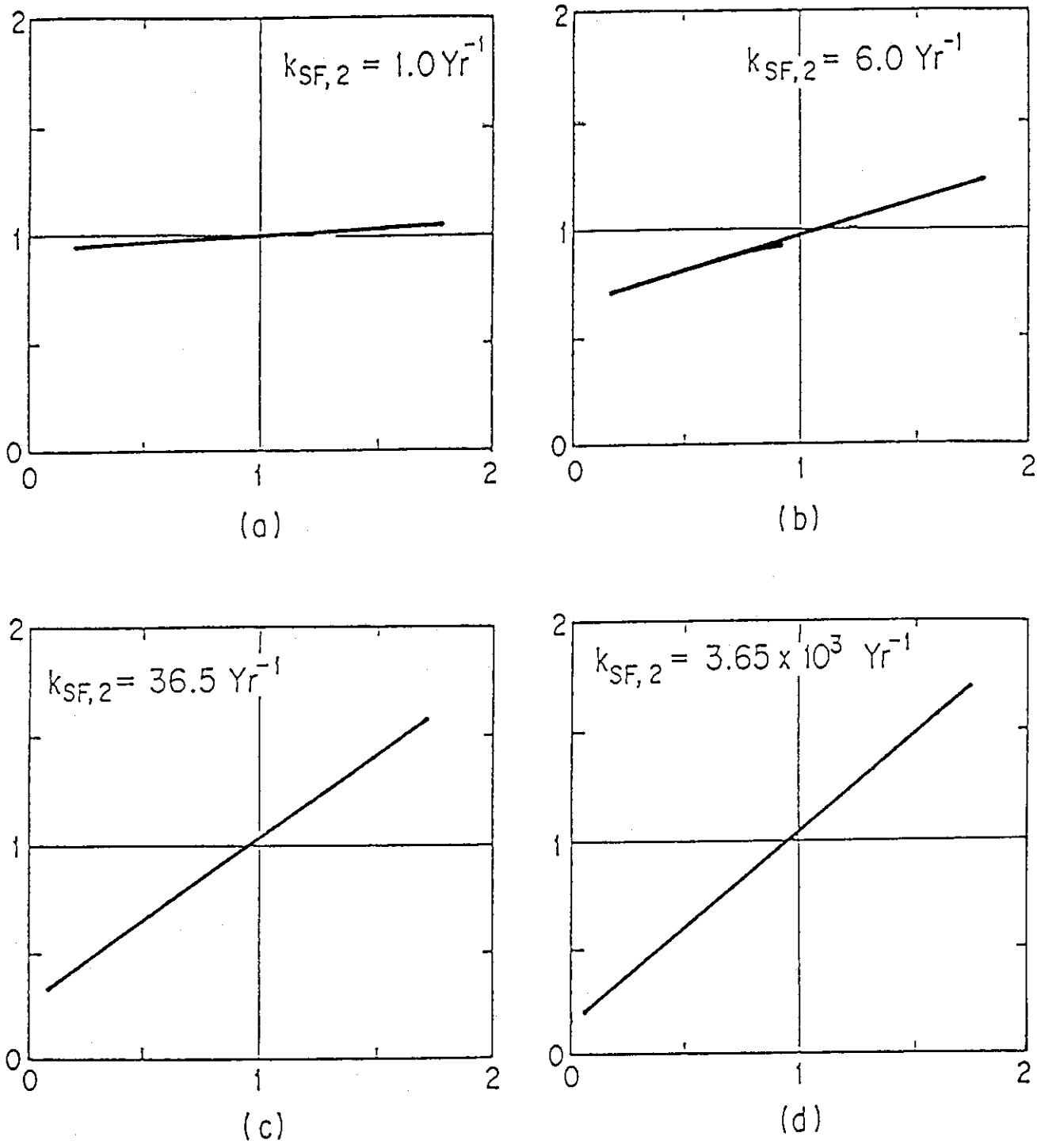

Fig. 4 The relationship between the $^{234}U/^{238}U$ and $^{230}Th/^{238}U$ activity ratios with the ^{234}Th fixation rates of 1.0 yr^{-1} (a), 6 yr^{-1} (b), 36.5 yr^{-1} (c), and 3.65×10^3 yr^{-1} (d).

3.2 Uranium Distribution in Mineral Species of Rock by Sequential Extraction Procedure

N. Yanase and H. Isobe

INTRODUCTION

Selective extraction procedures have been carried out for the rock samples at Koongarra to identify significant mineral species in which uranium accumulation and isotope disequilibrium have occurred. In the previous report[1], the uranium distributions in the mineral species were discussed on the basis of the mineral species of the rock determined by the visual observation. In this study the rock samples collected from the 6200N cross section were analyzed by the sequential extraction procedure and powder X-ray diffraction (XRD) analysis.

EXPERIMENTAL

The rock samples collected from the 6109N and 6200N cross sections were analyzed by the sequential extraction procedure. One g of a crushed material was sequentially treated by the extraction solutions (Table 2.1), and the residual minerals and liquid phases were separated by centrifugation and filtration using a 0.45 μm Millipore filter[2].

After adding ^{232}U tracer, uranium was separated from thorium and the other alpha emitters by an anion exchange resion (AG1×8, 100-200 mesh), followed by iron removal using a di-isopropyl ether extraction[3]. The uranium was then electroplated onto a stainless steel disk and measured by alpha spectrometry using a silicon surface barrier detector.

Uranium distributions and $^{234}U/^{238}U$ and $^{230}Th/^{234}U$ activity ratios were discussed on the basis of the mineral species of the rock samples. The mineral species of the rock samples including the previous samples, were determined by XRD analysis. The mineral species dissolved by the five-stage sequential extraction procedure were also examined for two rock samples containing uranium minerals by analyzing the residues after each extraction by XRD analysis.

RESULTS AND DISCUSSION

Effect of extraction reagents to the mineral species

The possible minerals dissolved by the extraction reagents are as follows:

1) Adsorbed trace materials and carbonate minerals. Morgan[4] used a 1 M NaOAc (pH 5.0) for dissolving carbonate minerals. Since exchangeable metals are removed by 1 M NaOAc (pH 8.2), they are perhaps included in Morgan's fraction if Morgan's solution is selected as the first extraction step. Payne[5] carried out adsorption and subsequent desorption experiments using ^{236}U for the natural rock, and found that most of the ^{236}U adsorbed onto the rock surface, was removed in Morgan's fraction.

2) Ferrihydrate, amorphous minerals of Fe, Al and Si, and secondary U minerals. Tamm[6] used an acid oxalate for dissolving amorphous minerals and ferrihydrite. Chao et al.[7] investigated the dissolution of amorphous and crystalline iron oxides by Tamm's solution and reported that 42% (natural) and 73% (synthetic) of amorphous iron oxides, 17 to 20% of magnetite, and less than 1% of hematite and goethite were dissolved after 4 hours reaction in the dark. Iron-rich chlorite, biotite and illite were also attacked by Tamm's solution[8]. Figure 2.1 shows the effect of sequential extraction on the minerals in the DDH1 sample (19.4-20.5 m) by XRD analysis. It can be seen that sklodowskite ($Mg(UO_2)_2(SiO_3OH)_2$% $5H_2O$) is dissolved by Tamm's solution[2].

3) Crystalline iron minerals. Hematite[8] and goethite[8,9,10] were dissolved by the CDB solution. However, clays and quartz were not affected[9,10].

4) Clays, uranium oxides and some refractory minerals, Mehra et al.[8] reported that 7 to 12% of hematite and 18% of goethite were dissolved by hot 4 M HCl after 30 min reaction. Figure 2.2 shows the effect of sequential extraction on the minerals in the sample DDH2 (33.0-34.3 m) by XRD analysis. It can be seen that pitchblende ($UO_{2.25}$) and clay minerals (kaolinite, smectite and vermiculite) are dissolved, but quartz, mica and zeolite are not affected by the 6 M HCl extraction[2].

5) All remaining resistant minerals. As shown in Fig. 2.1 and Fig. 2.2, quartz, mica and zeolite still remain in the resistant mineral species[2].

Distribution of uranium in the mineral species of the rock samples

Quartz, mica, zeolite, clay minerals (smectite, vermiculite and kaolinite), iron minerals (hematite and goethite), and uranium minerals (pitchblende and sklodowskite), are the major minerals in the rock samples.

The typical distribution of uranium amongst the mineral species of the rock samples as determined by the sequential extraction procedure is given in Fig. 2.3. In the secondary ore body, most of the uranium was contained in the CDB fraction (42-60%) of all the rock samples, suggesting the closest association of uranium with hematite and goethite.

In the primary ore body, 72% of the total uranium in DDH1 (19.4-20.5 m) was incorporated with the Tamm's solution extractable minerals (Fig. 2.3). This rock sample contains sklodowskite which is dissolved by the Tamm's solution as shown in Fig. 2.1. Therefore a large amount of the uranium in the Tamm's fraction result from the dissolution of sklodowskite.

For the deeper sample DDH2 (33.0-34.3 m), 70% of the total uranium was extractable with 6 M HCl (Fig. 2.3). The sample DDH2 (33.0-34.3 m) consists of clay minerals (kaolinite, smectite and vermiculite), pitchblende, quartz, mica and zeolite. Pitchblende is dissolved by 6 M HCl (Fig. 2.2), hence a large amount of the uranium in the 6 M HCl fraction probably results from the dissolution of pitchblende.

U-234/U-238 activity ratios of the mineral species of the rock samples

The $^{234}U/^{238}U$ activity ratios of the extracted fractions are shown in Fig. 2.4. In the secondary ore body and the shallow region of the primary ore body, DDH1 (19.4-20.5 m), the $^{234}U/^{238}U$ activity ratios of the fusion fractions are significantly greater than unity (2.8-6.3). Alpha recoil processes leading to enrichment of ^{234}U in mineral species have been proposed by Rosholt[11]. From its mechanism resistant mineral species in the rock at Koongarra seem to be surrounded by uranium-rich mineral species and isolated from the groundwater.

The $^{234}U/^{238}U$ activity ratios in the fusion fractions of the sample DDH2 (33.0-34.3 m) in a deeper region of the primary ore body, and DDH87 (24.3 m) under the secondary ore body are unity, hence ^{234}U enrichments do not occur in resistant mineral species of these samples. Only these samples do not contain highly uranium-associated minerals such as sklo-

dowskite, and hematite and goethite produced by the alteration of uraninite and chlorite, respectively. Resistant mineral species in these samples seem not to be surrounded by uranium-rich minerals.

REFERENCES

1. Yanase, N. (1990): Uranium Distribution in Mineral Phases of Rock by a Five Phase Sequential Extraction Procedure, Alligator Rivers Analogue Project, 1st Annual Report, 1989-90, ANSTO.
2. Yanase, N., Nightingale, T., Payne, T. and Duerden, P.: Uranium Distribution in Mineral Phases of Rock by Sequential Extraction Procedure, Radiochim. Acta 52/53, 387(1991).
3. Airey, P.L., Roman, D., Golian, C., Short, S., Nightingale, T., Lowson, R.T. and Calf, G.E.: Radionuclide Migration Around Uranium Ore Bodies - Analogue of Radioactive Waste Repositories, USNRC Contract NRC-04-81-172, AAEC Annual Report 1981-82, AAEC/C29 (1982).
4. Morgan, M.F.: The Universal Soil Testing System. Connecticut Agricultural Experiment Station Bulletin 372(1935).
5. Airey, P.L., Roman, D., Golian, C., Nightingale, T., Payne, T., Duerden, P., Davey, B.G., Gray, D. and Lever, D.A.: Radionuclide Migration Around Uranium Ore Bodies - Analogue of Radioactive Waste Repositories, USNRC Contract NRC-04-81-172, AAEC (Aust. At. Energy Comm.) Annual Report, 1984-85, AAEC/C55, NUREG/CR-5040(1985).
6. Tamm, O.: Uber die Oxalatmethode in der Chemischen Bodenanalyse, Fran Statens Skogsforsoeksans, Stockholm, 27, 1(1932).
7. Chao, T.T. and Zhou, L.: Extraction Techniques for Selective Dissolution of Amorphous Iron Oxides from Soils and Sediments, Soil Sci. Soc. Am. J. 47, 225(1983).
8. Mehra, O.P. and Jackson, M.L.: Iron Oxide Removal from Soils and Clays by a Dithionite-Citrate System buffered with Sodium-Bi-Carbonate, 7th Nat. Conf., Clays Clay Miner., Monograph No.5, p.317(1960).
9. Airey, P.L., Roman, D., Golian, C., Short, S., Nightingale, T., Lowson, R.T. and Calf, G.E.: Radionuclide Migration Around Uranium Ore Bodies - Analogue of Radioactive Waste Repositories., USNRC Contract NRC-04-81-172, AAEC (Aust. At. Energy Comm.) Annual Report, 1982-83, AAEC/C40, NUREG/CR-3941(1984).
10. Lowson, R.T., Short, S.A., Davey, B.G. and Gray, D.: $^{234}U/^{238}U$ and

$^{230}Th/^{234}U$ Activity Ratios in Mineral Phases of a Lateritic Weathered Zone, Geochim. Cosmochim. Acta 50, 1697(1986).

11. Rosholt, J.N.: Isotopic Composition of Uranium and Thorium in Crystalline Rocks, J. Geophys. Res. 88, 7315(1983).

Table 2.1 Reagents and conditions used in sequential extraction procedure

Reagent	Minerals dissolved	Extraction condition
(1) Morgan's solution[1)] 1 M NaOAc, ajusted to pH 5.0 with HOAc.	Carbonate minerals. Adsorbed trace materials.	40 ml/g-sample. Shaken for 4 hours.
(2) Tamm's acid oxalata(TAO)[2)] 10.9 g/l oxalic acid, 16.1 g/l ammonium oxalate	Ferrihydrate. Amorphous minerals of Fe, Al and Si. Secondary U minerals (uranyl phosphate and silicate etc.).	40 ml/g-sample. Shaken in the dark for 4 hours.
(3) CDB solution Sodium dithionite 1 g/g-sample, 0.3 M tri-sodium citrate, 0.2 M sodium hydrogen carbonate at pH 8.5.	Crystalline iron oxides (hematite, goethite etc.)	60 ml/g-sample. Heated (85°C) and stirred for 30 min. The procedure was then repeated.
(4) 6M HCl	Clay minerals (vermiculite, smectite, kaolinite etc.). Uranium oxide.	Heated (85°C) and stirred for 2 hours.
(5) Digestion and fusion	All remaining resistant minerals (Quartz, mica etc.).	Evaporate to dryness with $HF/HClO_4$ followed by fusion in sodium carbonate and borax.

1) Morgan, M.F., Connecticut Agricultural Experiment Station Bulletin 372(1935).
2) Tamm, O., Fran Statens Skogsforsoeksans, Stockholm, 27, 1(1932).

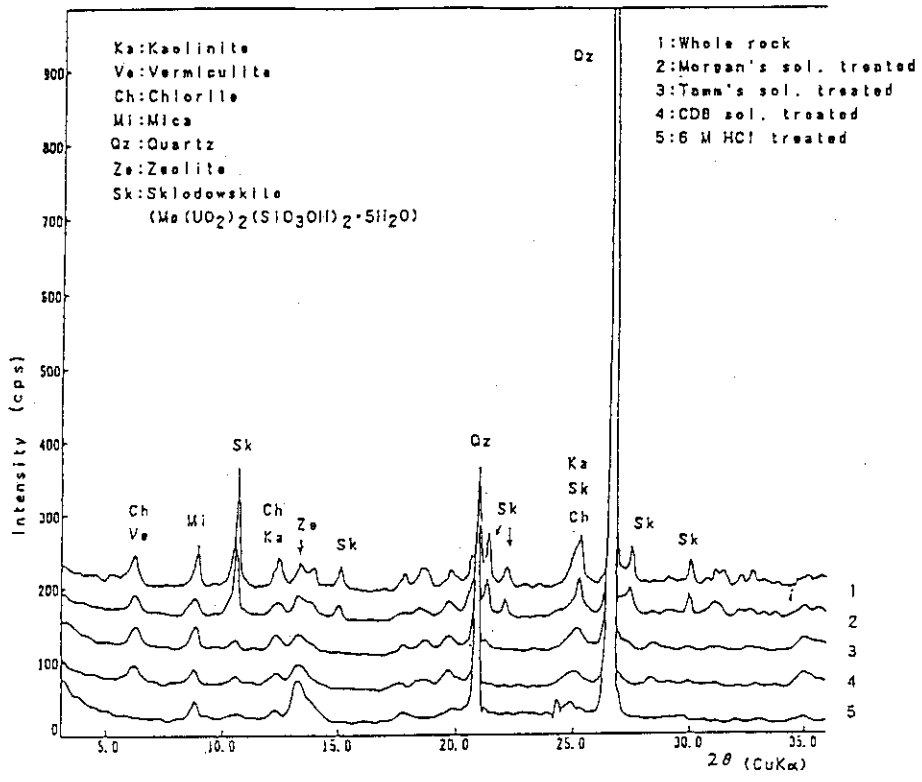

Fig. 2.1 Effect of sequential extraction to the minerals in the 19.4-20.5 m region of the drill hole DDH1 by XRD analysis.

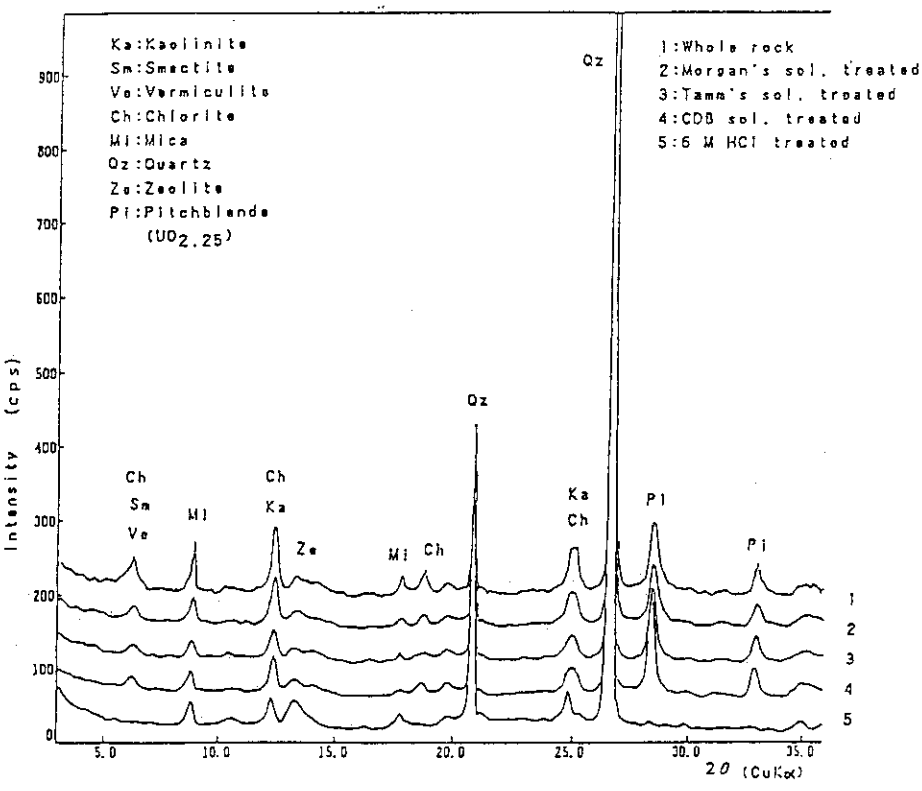

Fig. 2.2 Effect of sequential extraction to the minerals in the 33.0-34.3 m region of the drill hole DDH2 by XRD analysis.

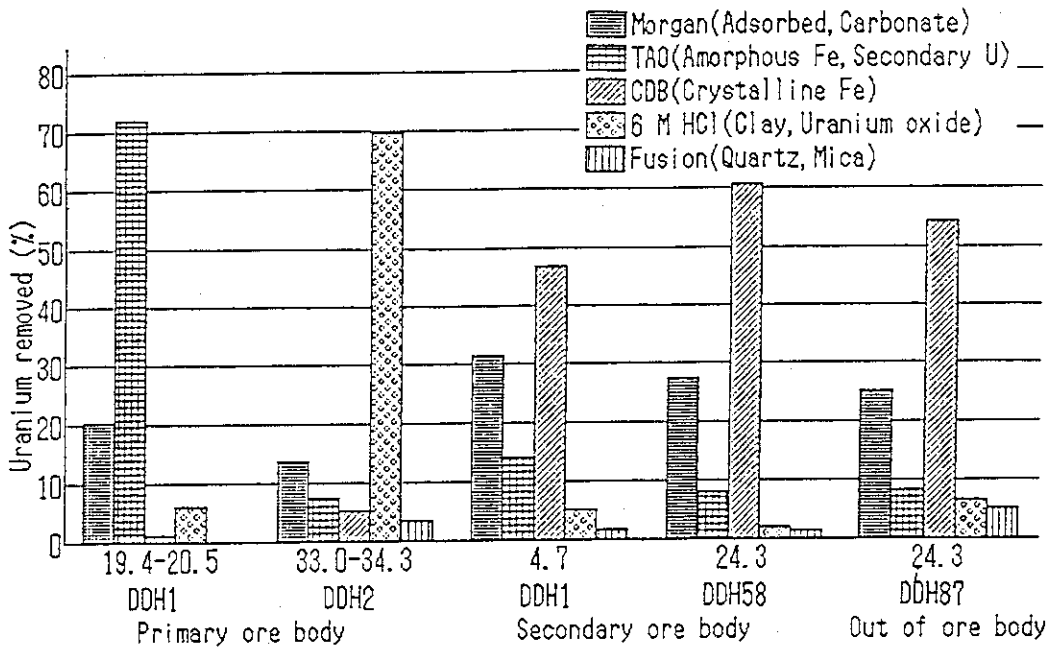

Fig. 2.3 Distribution of uranium in extracted phases.

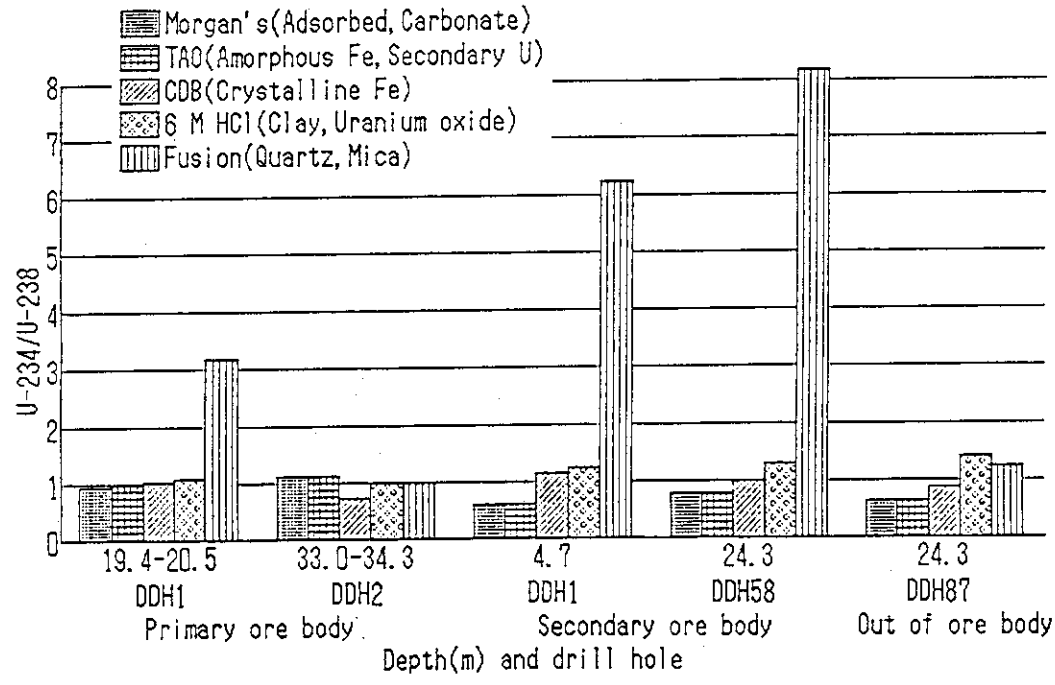

Fig. 2.4 Measured $^{234}U/^{238}U$ activity ratios in extracted phases.

3.3 Effects of Chlorite Alteration on Uranium Redistribution in Koongarra, Australia

T. Murakami, H. Isobe and R. Edis*

INTRODUCTION

At Koongarra in the Northern Territory of Australia, quartz-chlorite schist, the ore host rock, has been subjected to alteration (or weathering). In the weathered zone, quartz has persisted through the alteration process while chlorite has been altered to clay minerals and iron minerals[1] (See reference 2 for a detailed description of the geology and mineralogy of Koongarra). The region of secondary uraium, which has been formed by weathering of the primary ore and precipitation of secondary minerals, is located in the weathered zone but not in the unweathered zone where chlorite remains unaltered. Uranium is found as uranium oxides, uranium silicates, and uranium phosphates in the two ore regions, and associated with the alteration products of chlorite downstream of the secondary ore deposit[1]. The latter case is similar to that of the radionuclide migration which may follow the disposal of high level radioactive waste, in which the release of actinides, long-lived, hazardous radionuclides, may continue over geologic time.

The structurally and chemically altered minerals are metastable, and may take 10^5 to 10^6 years to become the final products of the alteration. Hence, the uranium series nuclides flowing from a source, react with the then coexisting minerals which vary with time as a function of the alteration mechanisms and kinetics. For example, when a uranium containing mineral is altered, one portion of the U is desorbed whilst the other is part is reaccommodated in another mineral being formed. This suggests that the retardation of the uranium series nuclides varies with time, that is, with the coexisting minerals. Therefore, a knowledge of the alteration mechanisms and kinetics is indispensable if we are to understand radionuclide migration over long, geologic time. The present paper demonstrates evidence of the effects of the alteration on uranium redistribution by comparing the mineralogical textures with alpha-track distributions of the Koongarra samples.

* Australian Nuclear Science and Technology Organization, PMB 1, Menai, NSW 2234, Australia

reveals that reprecipitation of the iron phase takes place out of the original chlorite, and that the Fe diffuses between the chlorite and vermiculite slabs during the transformation. Because U in the weathered zone is highly associated with the iron minerals[4,5], the distribution of the iron minerals between the constituent minerals at the various stages of the alteration needs to be understood more precisely for a better understanding of the uranium redistribution.

In a later stage of the alteration, kaolinite and smectite occur as sub-micron grains and the grains do not have any common crystallographic orientation. We have not found any evidence of textural relationships between kaolinite and chlorite or vermiculite.

The relative abundances of chlorite, vermiculite, and kaolinite were estimated as a function of depth on the basis of the XRD intensities; to simplify the calculation we used the XRD peak heights instead of the intensities. The chlorite peaks of DDH3-143 were taken as a standard for the chlorite peak profile because this chlorite showed no indication of alteration by XRD and little, by OM. The regular change in the intensity ratio at 1.4 nm to 0.7 nm when heating the chlorite to 450°C was used to calculate the amount of vermiculite present in a sample; note that vermiculite peaks disappear when a sample is heated to 450°C. Details of the calculation will be given elsewhere[3]. Mica and smectite were ignored in the calculation. If a sample was a mixture of chlorite and vermiculite, or of vermiculite and kaolinite, the method was applied. The relative abundances of chlorite, vermiculite, and kaolinite along the DDH3 corehole are given in Table 1. The chlorite, which is not al-

Table 1 Relative mineral abundances (%) of chlorite, vermiculite, and kaolinite along the DDH3 core

Sample	Depth	Chlorite	Vermiculite	Kaolinite
DDH3-75	17.5	0	0	100
DDH3-81	18.9	0	0	100
DDH3-88	20.5	0	20	80
DDH3-94	21.9	0	40	60
DDH3-103	24.0	0	80	20
DDH3-105	24.5	80	20	0
DDH3-111	25.9	100	0	0
DDH3-143	33.4	100	0	0

EXPERIMENTAL

For the present study twenty samples were collected from within and below the weathered zone. All but one were obtained by diamond drilling (referred to as DDH); the remaining sample resulted from percussion drilling. The samples were examined by X-ray diffraction analysis (XRD), optical microscopy (OM), scanning electron microscopy (SEM), and electron microprobe analysis (EMPA). The details of the XRD, SEM, and EMPA procedures will be described elsewhere[3].

Following the mineralogical observation, some of the samples were then examined by α-particle autoradiography. Films (Lexan polycarbonate plastic) were placed on the samples for 12 to 15 days, and etched with 6.25 M NaOH at 75°C for 6 hours. The films were then compared to their corresponding thin sections.

ALTERATION OF CHLORITE

The results of the XRD studies can be summarized as following; the degree of chlorite alteration varies as a function of depth; chlorite is transformed to vermiculite through regularly interstratified chlorite/vermiculite; vermiculite is converted to kaolinite and probably smectite; an iron mineral, possibly ferrihydrite, is formed during the alteration; and goethite and hematite are also found in the weathered zone. At Koongarra, the successive process of alteration as a function of depth may correspond exactly to one of time. Two micas, muscovite and biotite are often found by OM and XRD and like chlorite, they can be converted to vermiculite. However, as the amounts of the two micas are small in the downstream region of the secondary ore deposit, we can ignore their influence in the following discussion of alteration.

With the proceeding alteration of chlorite to vermiculite, the grains of altered chlorite (seen as a layer texture in SEM images) consist of slabs of chlorite and vermiculite 1 μm thick. Between the slabs, an iron phase (possibly ferrihydrite) occurs as short slabs. The layered texture suggests that the crystallographic orientation of the chlorite structure is retained during the transformation of chlorite to vermiculite. In a later stage of the transformation, the iron phase is accumulated between the vermiculite slabs. The occurrence of the iron phase

tered even at 111 feet along the DDH3 core (25.9 m deep from the surface vertically), rapidly decreases between 107 and 103 feet (25 and 24 m deep) and disappears above 103 feet. Vermiculite appears at 107 feet (25 m deep) and is at a maximum at 103 feet (24 m deep) where kaolinite begins to persist. Vermiculite disappears at 86 feet (20 m deep) where kaolinite is predominant as it is in the shallower zone.

The comparison of the mineral abundances to the uranium concentrations and their close relationship has been reported previously[11]; the chlorite predominant zone corresponds to the zone of lower uranium concentrations, the vermiculite predominant zone, to the zone of intermediate uranium concentrations, and the kaolinite predominant zone, to the zone of highest uranium concentrations.

URANIUM DISTRIBUTION IN THE MINERALS

Prior to sampling, we inspected the diamond-drilled cores, and found that alteration was always initiated at fractures in the rock. Samples containing fractures were chosen for an α-particle autoradiography examination of the qualitative distribution of uranium between the constituent minerals and the textures.

The DDH6-99 sample contains a fracture which intersects the schistosity (running from left to right in Fig. 1a). Along the fracture, the sample has a highly altered zone (up to 1.3 mm thick), and a 2 mm thick chlorite alteration zone. In the altered zone, chlorite is altered to clay minerals (an OM examination could not distinguish between vermiculite, kaolinite, and smectite) and the iron minerals. Some of the chlorite outside the altered zone is slightly brown, i.e., partially altered. This suggests that the fractures are preferential pathways of water, the chlorite is altered initially along the fractures, and thus, the alteration resulting from the water-rock interaction is a kind of "fossil" of the past water path.

The α-particle track map corresponding to the DDH6-99 thin section (Fig. 1b) shows that the tracks are highly concentrated along the fracture and also homogeneously distributed, though at far lower density, in other areas, excepting the quartz grains. This strongly suggests that the uranium concentration of redistribution is closely related to the extent of the chlorite alteration; U is concentrated in more altered

chlorite. In comparison with the α-particle track density of an unaltered sample (DDH3-111.5, 26 m deep), the tracks of DDH6-99 indicate that U (as well as water) has penetrated even when chlorite is only slightly altered.

Figure 2 is a superimposition of the α-particle track film and the thin section of DDH4-100. A single open circle corresponds to one α-particle track. The area shown in Fig. 2 is a 3 mm section from a fracture along which chlorite is highly altered, similar to that of Fig. 1a. Because the black areas are past grain boundaries of chlorite, the figure indicates that the chlorite grain boundaries are another preferential pathway for water, and that U is concentrated in the most highly altered part, viz the grain boundaries.

Figure 3 is a superimposition of the α-particle track film and thin section of DDH3-100. In the upper part of Fig. 3, the grains shown as white are quartz, and in the lower part, the gray areas are micas and chlorite; the black areas are highly altered micas and chlorite. The α-particle tracks are found on the black materials (opaque by OM) between the quartz grain boundaries (a thick arrow in Fig. 3), and on the altered chlorite and micas (a thin arrow in Fig. 3). The black materials between the quartz boundaries suggest that the grain boundaries of quartz are preferential pathways for water although quartz itself is a stable phase. If the black materials are iron minerals, then Fe has been transported by water. More importantly, such (black) materials are good adsorbants of U. It is again confirmed in this figure, that uranium redistribution is related to the degree of chlorite alteration.

The black curves in Fig. 4a, indicate a network of microfissures where highly altered chlorite and micas are seen. The corresponding α-particle track map shows that U is concentrated along the microfissures (Fig. 4b), with the tracks being seen even in quartz grain boundaries (left and upper part of Figs. 4a and 4b). As mentioned above, alteration occurs as a function of depth. However, when fractures and/or microfissures are formed locally, chlorite is subjected to increased local alteration and U is more highly concentrated in the altered area.

SUMMARY AND CONCLUSIONS

The alteration of chlorite occurs as a function of depth; chlorite

is transformed to vermiculite, through regularly interstratified chlorite/vermiculite. The Fe released from chlorite reprecipitates to form iron minerals, possibly ferrihydrite. Vermiculite is then replaced by kaolinite (and possibly smectite), further releasing Fe. On the millimetre scale, an α-particle autoradiography study has shown that uranium concentrations are qualitatively proportional to the extent of the alteration; altered chlorite grains having higher uranium concentration. On the metre scale, the X-ray diffraction study has revealed that the abundances of chlorite, vermiculite, and kaolinite correspond well to the low, intermediate, and high uranium concentration zones, respectively. This strongly suggests that the process, mechanisms, and kinetics of chlorite alteration affect the uranium migration at Koongarra.

Our results suggest that the mechanism for uranium migration varies with "geologic" time as a consequence of geochemical processes such as alteration, a slow reaction. The study of chlorite alteration demonstrates the importance of the processes, mechanisms, and kinetics of alteration (or weathering) in radionuclides migration through rock surrounding disposal sites.

REFERENCES

(1) A.A. Snelling, Uraninite and its alteration products, Koongarra uranium deposit, in Proceedings of IAEA International Symposium Uranium in the Pine Creek Geosyncline, edited by J. Ferguson and A.B. Goleby (IAEA, Vienna 1980) pp. 487-498.

(2) A.A. Snelling, Koongarra uranium deposits, in The Geology of the Mineral Deposits of Australia and Papua New Guinea, Monograph 14, edited by F.E. Hughes (The Australian Institute of Mining and Metallurgy, Melbourne) (in press).

(3) H. Isobe and T. Murakami, Alteration of chlorite and its relevance to uranium migration (in preparation).

(4) P.L. Airey, Radionuclide migration around uranium ore bodies in the Alligator Rivers Region of the Northern Territory of Australia-Analogue of radioactive waste repositories - A review. Chem. Geol. 55, 255 (1986).

(5) P.L. Airey and M. Ivanovich, Geochemical analogues of high-level radioactive waste repositories. Chem. Geol. 55, 203 (1986).

(6) T. Murakami and H. Isobe, Alteration of chlorite and its relevance to uranium migration, Alligator Rivers Analogue Project 1st Annual Report 1988-89, edited by P. Duerden (ANSTO, Australia, 1990) pp. 113-118.

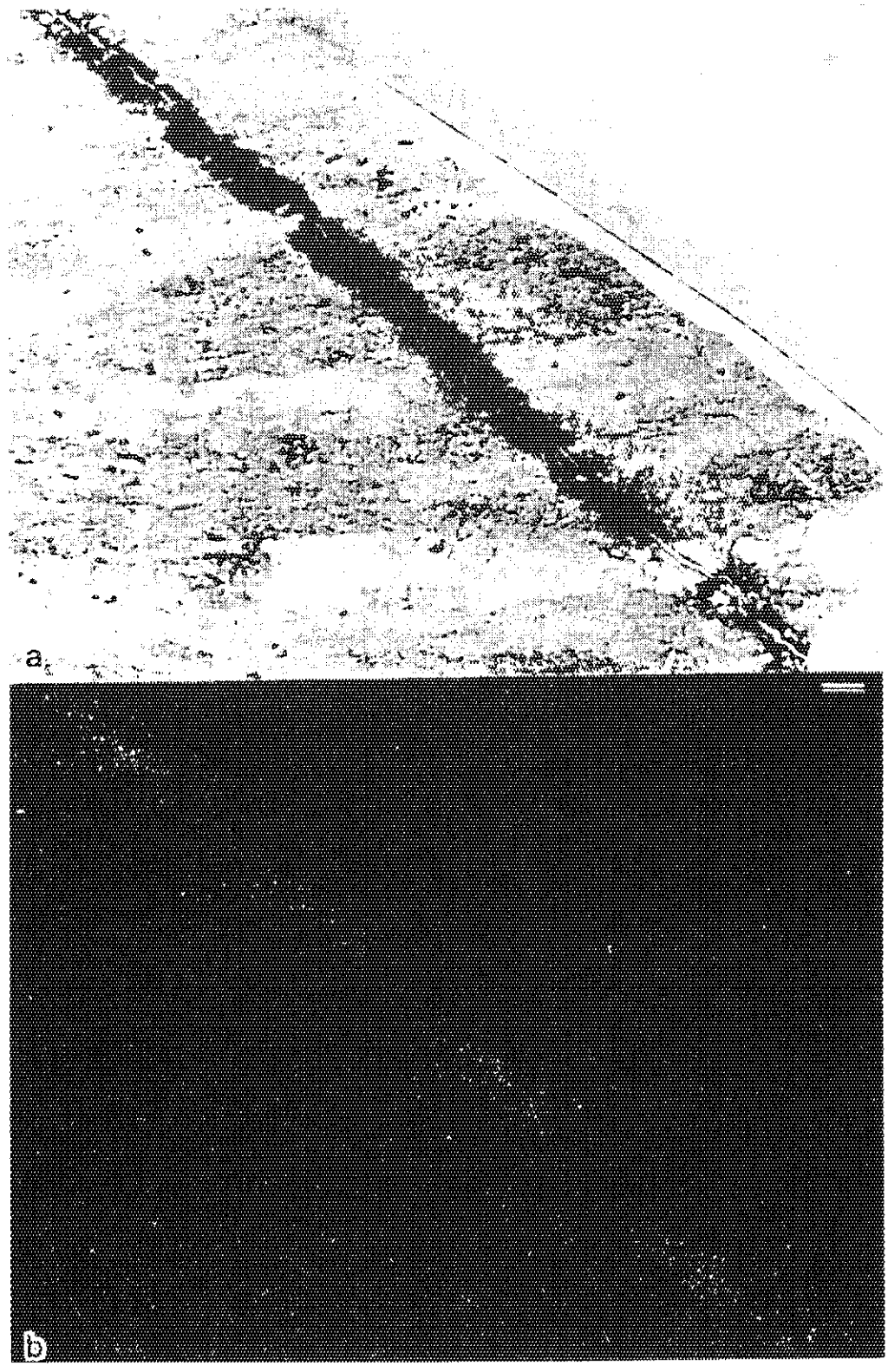

Fig. 1 Micrograph (a) and its corresponding α-particle track map (b) of DDH6-99. The white line from the upper left to the bottom right is a fracture along which chlorite is strongly altered (indicated by a black zone). White zones running from the right to left consist of quartz grains and gray areas, mostly chlorite grains. A bar indicates 1 mm.

Fig. 2 Superimposition of the α-particle track film and thin section of DDH4-100. Altered chlorite grains are in gray, and quartz grains, in white. The open circles are α-particle tracks. A bar indicates 1 mm.

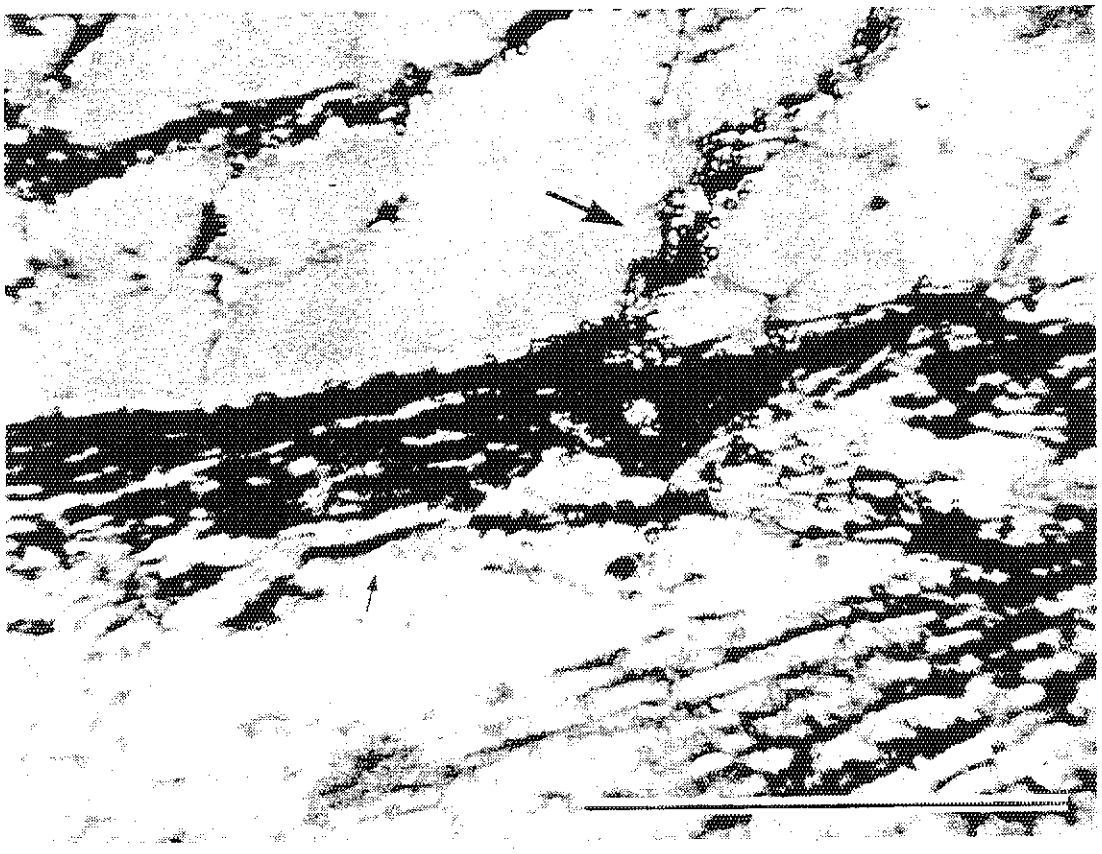

Fig. 3 Superimposition of the α-particle track film and thin section of DDH3-100. White grains in the upper part are quartz and altered micas and chlorite are in the lower part. A thick arrow indicates black material precipitation and a thin arrow, highly altered chlorite and micas. A bar indicates 1 mm.

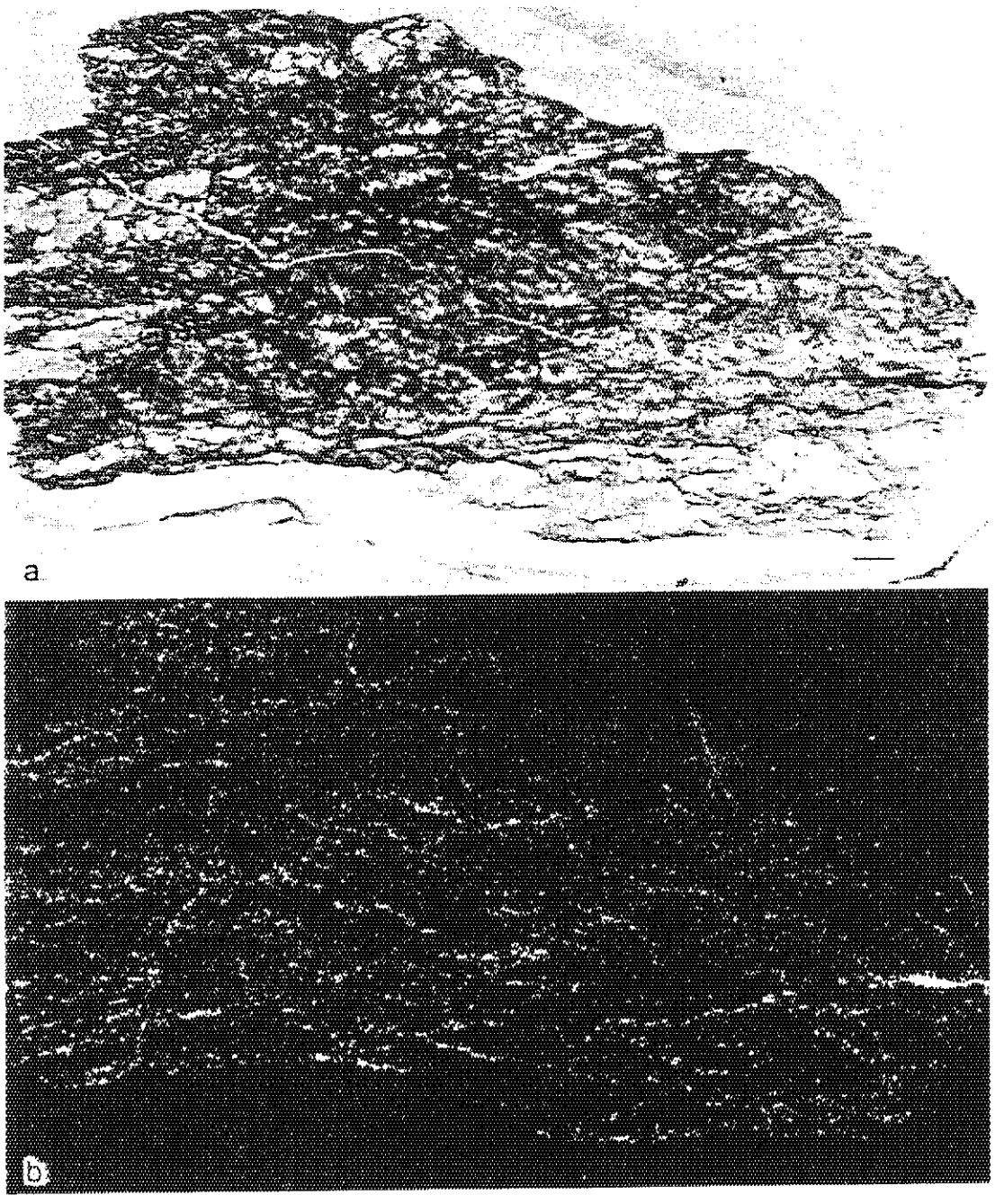

Fig. 4 Micrograph (a) and its corresponding α-particle track map (b) of DDH3-104. Note that the fracture in the middle running from the left to right was possibly made during the sample preparation. A bar indicates 1 mm.